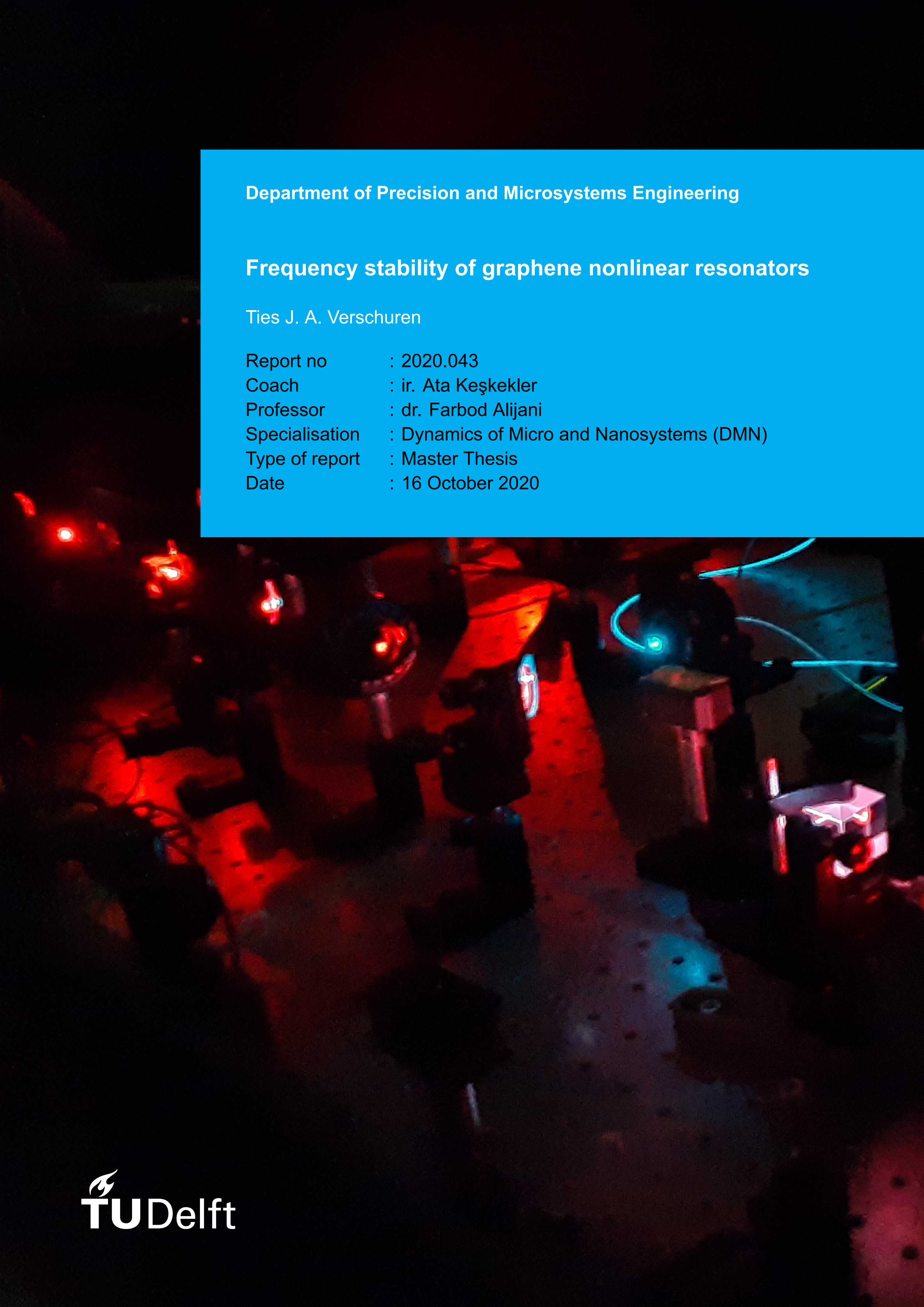

Department of Precision and Microsystems Engineering

Frequency stability of graphene nonlinear resonators

Ties J. A. Verschuren

Report no : 2020.043
Coach : ir. Ata Keşkekler
Professor : dr. Farbod Alijani
Specialisation : Dynamics of Micro and Nanosystems (DMN)
Type of report : Master Thesis
Date : 16 October 2020

Frequency stability of graphene nonlinear resonators

Master thesis

by

Ties J. A. Verschuren

to obtain the degree of Master of Science
at the Delft University of Technology,
to be defended publicly on Friday October 16, 2020 at 1:00 PM.

Student number:	4343670	
Project duration:	September 2, 2019 – October 16, 2020	
Thesis committee:	Dr. Farbod Alijani,	TU Delft, supervisor (chair)
	Ir. Ata Keşkekler	TU Delft, daily supervisor
	Dr. Richard Norte	TU Delft
	Dr. Tomás Manzaneque García	TU Delft

This thesis is confidential and cannot be made public until October 16, 2022.

TU Delft

Abstract

In pursuit of extremely sensitive sensors, the dimensions of these devices get smaller and smaller. Small scale resonators are commonly used as sensors by relating changes in the dynamic behaviour to a sensed quantity. Conventionally, the dynamics used for sensing are in the linear regime. However, at smaller scales the dynamic range of the linear regime decreases. Therefore, it is of interest to investigate the dynamic behaviour in the nonlinear regime, as with the decreasing scale of the resonators this becomes inevitable. Especially, little is known about the frequency stability in this region. The frequency stability provides an indication for the potential sensitivity that the resonator can have as sensor. By using phase locked loop (PLL) the frequency stability around the resonance frequency of nonlinear resonators can be obtained. This research contains attempts to control multilayer graphene drums around its fundamental resonance frequency with PLL. In addition, the frequency stability at these points are presented by measure of the Allan Deviation. It is found that the frequency stability is the best within the bistable regime. One resonator shows behaviour attributed to internal resonance. This internal resonance is linked to an increase of nonlinear damping. Combining that with a single degree of freedom simulation model, a relation was found between increased nonlinear damping and an improvement of frequency stability.

Preface

As an engineer-in-the-very-near-future, I believe in a certain malleability in the domain of mechanical engineering. So, when I discussed with Farbod about potential graduation projects, I immediately became enthusiastic about this project. It would be super cool to stabilize the unstable branch of a Duffing resonator and this way making sure the amplitude jumps become history. Next to that, it would pave the way to numerous sensing applications. The result of my enthusiasm at that moment is the thesis in front of you.

Of course, my enthusiasm has faded from time to time during this project. Endless mathematical derivations that are impossible to get through, a global pandemic, days when nothing works out in the lab, many measurement results but no conclusion and writing it all down as clearly as possible are examples of when that happened. However, there are a lot of people to talk to within the Dynamics of Micro- and Nanosystems group and their experience helped me further. Thank you for the helpful discussions and hints, Ata, Farbod, Tomás, Irek and Richard! Something I really appreciated were the weekly meetings with Ata and biweekly meetings with Farbod and Richard. This way I was always sure I was on the right track.

These last weeks I ”drained the rock” as Ata would say, to get it all done. This would not have been possible without the help of others. Therefore, I would like to thank my fellow peers, those I worked with during our graduation projects. My parents and brother for trying to understand what I was working on. And finally, I would like to thank my girlfriend for surviving to live with me when I had only time to work on my graduation project.

Finally, I address you, dear reader. Although this research is not perfect, I hope it will contribute to your attempts at malleability of mechanical systems.

Ties J. A. Verschuren
Delft, October 2020

Contents

1

Introduction

In recent decades, sensor development has led to increasingly sensitive sensors. Therefore, the quantities that can be measured become smaller and so do the sensors itself. One class of these small sensors are the resonant sensors. The working principle of these vibrating devices is the fact that the resonance frequency of the device changes when a quantity is sensed. The sensitivity of such devices can be improved by reducing their weight and by increase their resonance frequency [1]. This is where graphene comes into play.

Graphene is a thin sheet of graphite (same material as the core of a pencil) of only one atom layer thick. Graphene was discovered, in 2004 [2] and since then, a lot of research has been conducted on this new material and, remarkable mechanical properties were discovered. For example, its has a higher tensile strength than steel [3], but it weights a lot less [4]. Graphene can be used in sensitive sensors, to sense small quantities mass, pressure, strain, force or charge [5].

At micro- and nanoscale, the resonance frequency of graphene does not only depend on the mechanical properties of the resonator, but also on the vibration amplitude. This is called nonlinear dynamic behaviour. A characteristic aspect is the existence of three vibration amplitudes at certain frequencies, called the bistable region. Two of those amplitudes depend on the direction (increase or decrease) of the frequency that causes the resonator to vibrate. The third one is unstable and therefore unreachable by any frequency. One needs to understand the nonlinear dynamics in order to avoid or exploit these [6, 7].

Exploiting these nonlinear dynamics has become more of interest in the last years in pursuit of the practical limits of sensor performance. When scaling down the size of resonators, nonlinear behaviour becomes unavoidable. Understanding of these nonlinear phenomena has the potential to improve performance beyond what was conventionally considered possible [8].

To exploit the nonlinear behaviour, stabilizing the unstable branch in the bistable regime is of interest. The goal is to reach each vibration amplitude in this regime on command. This can be achieved by using a controller to drive the resonator. Specifically, a phase-locked loop can achieve this [9]. However, this is a challenge for graphene resonators due to their high resonance frequency and their strong damping. This means that the resonator can adapt fast to changes, so the controller should also be fast. This thesis shows that it is possible to overcome this challenge.

The sensitivity of a resonant sensor is also limited by the uncertainty of the measured resonance frequency [10].This can be quantified with the Allan deviation which is a measure for frequency stability. The frequency stability of graphene resonators is an underexposed topic in scientific literature. This thesis presents the frequency stability of graphene resonators around its resonance frequency. Furthermore, a relation between frequency stability and nonlinear damping is demonstrated. This shows that at certain operation points the frequency stability can be improved, which can lead to a sensitive sensor.

In the following sections, topics like resonators, difference between a linear and nonlinear resonator, frequency stability and PLL are explained in more detail. Next, the main findings of this thesis are

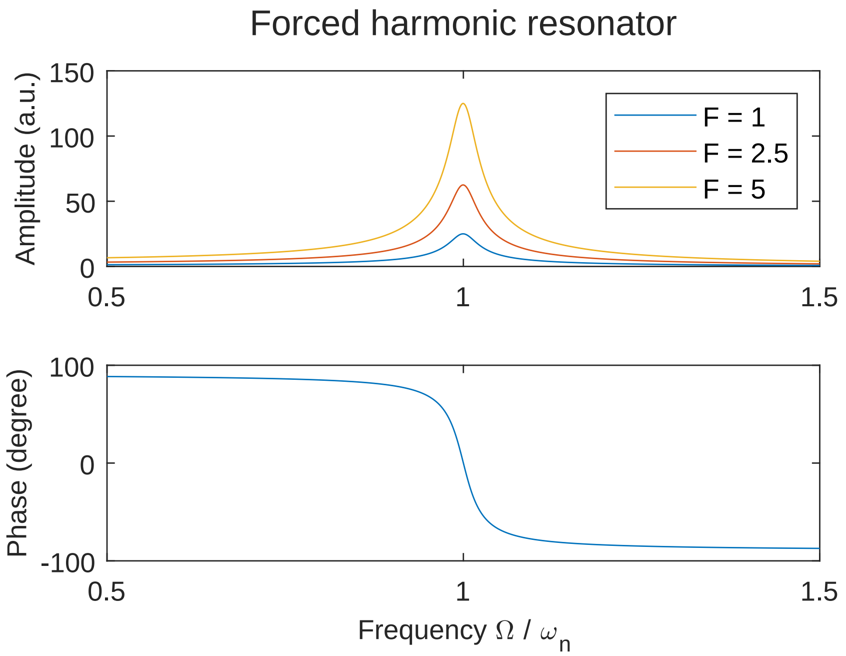

Figure 1.1: Frequency response for a linear resonator modelled as a forced harmonic resonator. Derivation of the amplitude and phase equations are presented in appendix D.1. The parameters used are $\zeta = 0.02$ and $\omega_n = 1$.

presented in a scientific paper format. The report concludes with recommendations for further research. Supporting material can be found in the appendices.

1.1. Resonators

When an ideal (lossless) mechanical structure is oscillating at its *eigenfrequency*, the total energy stored in the device consists solely of potential and kinetic energy. A vibrational mode () where this occurs is called an *eigenmode*. Continuum mechanical structures have many of these eigenmodes.

In a real mechanical structure, a very small amount of energy is lost during each vibration cycle, due to different dissipation mechanisms. In this case, the frequency at which the total energy is almost solely being transferred between potential and kinetic energy is called the *resonance frequency*. The phenomenon of eigenmodes in the ideal structures is called *resonance* in the real mechanical systems. The resonance frequency of the real mechanical structure is typically close to the eigenfrequency of the same structure assumed without losses [11]. Therefore, these terms are used interchangeably.

A mechanical system that shows distinct resonance is called a resonator. An oscillator on the other hand is a mechanical structure that exhibits vibrations without any oscillatory input. When a resonator is incorporated in a control loop (i.e. feedback is applied), it becomes an oscillator [12, 13].

When investigating resonance of a mechanical system, one typically looks at the frequency response, which is the vibration amplitude for different excitation frequencies. Amplitude peaks in the frequency response indicate the resonance frequencies. This frequency response can be obtained by either solving the differential equation or by taking the Fourier or Laplace transform from the resonator equation of motion [13].

In the next subsections, the frequency response of different resonator models is discussed.

1.1.1. Linear resonator

A linear resonator can be modelled as a forced harmonic excitation system [13, 14], see eq. (1.1) below.

$$\ddot{x} + 2\zeta\omega_n\dot{x} + \omega_n^2 x = F\cos(\Omega t) \tag{1.1}$$

The vibration amplitude is denoted by x, the resonance frequency by ω_n and the damping factor by

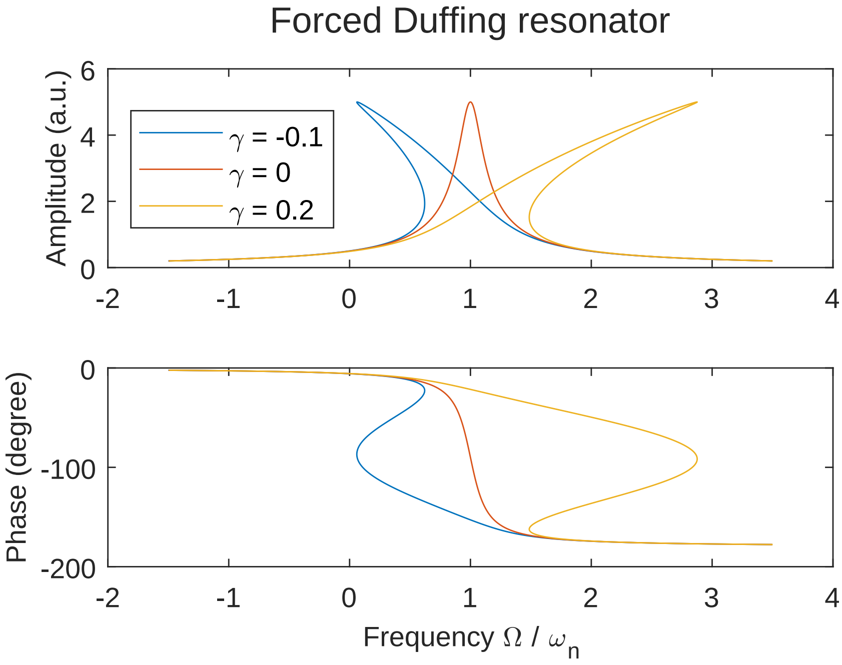

Figure 1.2: Frequency response of a forced Duffing resonator for different values of γ. The peak is linear (red) or shows softening (blue) or hardening (yellow) behaviour. Derivation of the amplitude and phase equation can be found in appendix D.2. The parameters used are $\zeta = 0.1$, $\omega_n = 1$ and $F = 1$.

ζ. The harmonic force amplitude and excitation frequency are indicated by F and Ω respectively. It can be seen from Eq. 1.1 that it concerns a linear resonator, as it contains only linear combinations of amplitude x and its time derivatives ($\dot{x}$ and $\ddot{x}$).

The frequency response of a linear resonator is presented in fig. 1.1, which shows that the resonance peak is symmetrical and the amplitude is proportional to the driving force.

1.1.2. Nonlinear resonator

The first eigenmode of a nonlinear resonator can be modelled as a forced harmonic Duffing resonator [15, 16], which can be described as in eq. (1.2).

$$\ddot{x} + 2\zeta\dot{x} + x + \gamma x^3 = F\cos(\Omega t) \tag{1.2}$$

The symbols x, ζ, F and Ω have the same meaning as with the linear resonator and eq. (1.2) is normalized with respect to ω_n compared to eq. (1.1). The characteristic part is the cubic term γx^3, where γ is known as the cubic stiffness. When this parameter is zero, it behaves like a linear resonator. If not, the frequency response of the Duffing resonator becomes a multivalued function of the frequency around its resonance peak, i.e. it is not a straight peak any more. Depending on the cubic stiffness this happens before ($\gamma < 0$, called softening) or after ($\gamma > 0$, called hardening) the linear resonance frequency, see fig. 1.2.

Within this multivalued region, there are 3 coexisting solutions for the resonator. This is also called the region of bi-stability because there are two stable solutions and one unstable solution. At the edges of this region, the periodic response of the resonator loses stability, causing a jump in amplitude and phase when sweeping the forcing frequency. In fig. 1.3 it is shown that the resulting amplitude and phase trajectory depends on the sweep direction [17].

1.2. Frequency stability

Oscillators and resonators exhibit a periodic signal with a certain frequency. For many applications, like clocks and sensors, it is important to know what the frequency stability of the resonance frequency

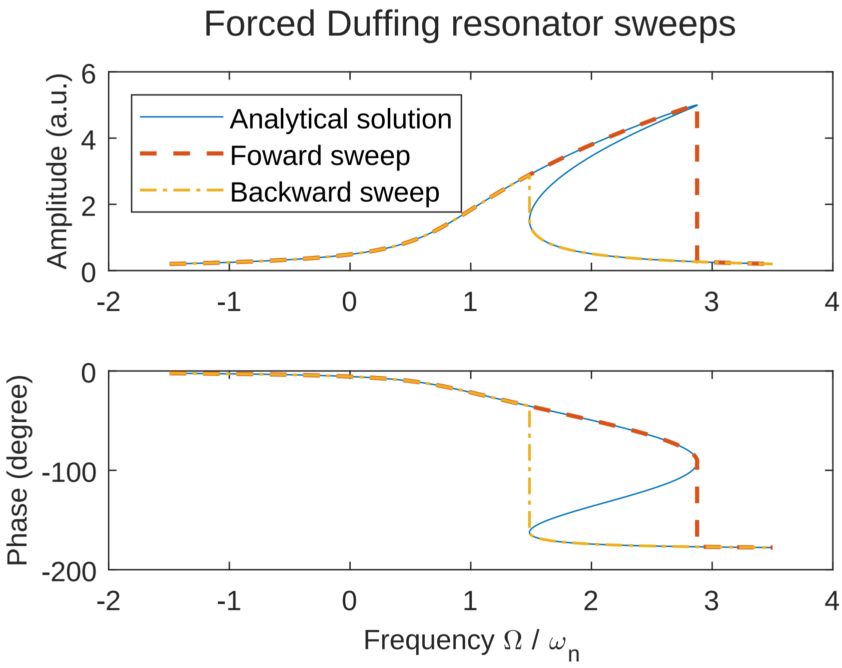

Figure 1.3: Forward and backward frequency sweep for a hardening Duffing resonator. In both the amplitude and phase a jump occurs when sweeping. The location of this jump differs for the forward and backward sweep.

is [18]. In other words, it answers questions like: how does the uncertainty of the measured frequency influence the minimal change in resonance frequency one can observe? And how many measurement samples are needed to have a sufficient frequency stability? All practical devices based on a resonator have finite frequency precision. As this defines the smallest detectable frequency change, it therefore defines the smallest change that a resonant sensor can sense. It is true that the smaller the uncertainty, the lower the Allan Deviation and the greater the frequency stability.

Therefore, it is interesting to express this frequency stability in numbers so different devices can be compared with each other. One method to quantify frequency stability is the Allan Deviation ($\sigma_y(\tau)$) [19], also known as the Allan Variance ($\sigma_y^2(\tau)$) . This is a time domain method. The Allan Variance is defined as the expectation (denoted by $\langle\rangle$) of the difference of two adjacent measurements.

$$\sigma_y^2(\tau) = \frac{1}{2}\langle(\bar{y}_{k+1}(\tau) - \bar{y}_k(\tau))^2\rangle \approx \frac{1}{2(N-1)}\sum_{k=1}^{N-1}\langle\bar{y}_{k+1}(\tau) - \bar{y}_k(\tau)\rangle^2 \tag{1.3}$$

The right part in eq. (1.3) is an approximation for a finite set of samples of y. Here is N the number of sequential adjacent samples.

To see how eq. (1.3) can be used, consider eq. (1.4) as the output of an oscillator [19].

$$V(t) = [V_0 + \epsilon(t)]\sin(\omega_0 t + \phi(t)) \tag{1.4}$$

V_0 and ω_0 are the nominal amplitude and frequency, and $\epsilon(t)$ and $\phi(t)$ are the fluctuations over time in amplitude and frequency respectively. This model assumes that there is no relation between the amplitude and frequency deviation [18]. In this case we are only interested in the frequency fluctuations. The actual frequency of the signal in eq. (1.4) is

$$\omega(t) = \omega_0 + \frac{d\phi(t)}{dt} \tag{1.5}$$

Next, the fractional frequency deviation is defined in eq. (1.6).

$$y(t) = \frac{\omega(t) - \omega_0}{\omega_0} \tag{1.6}$$

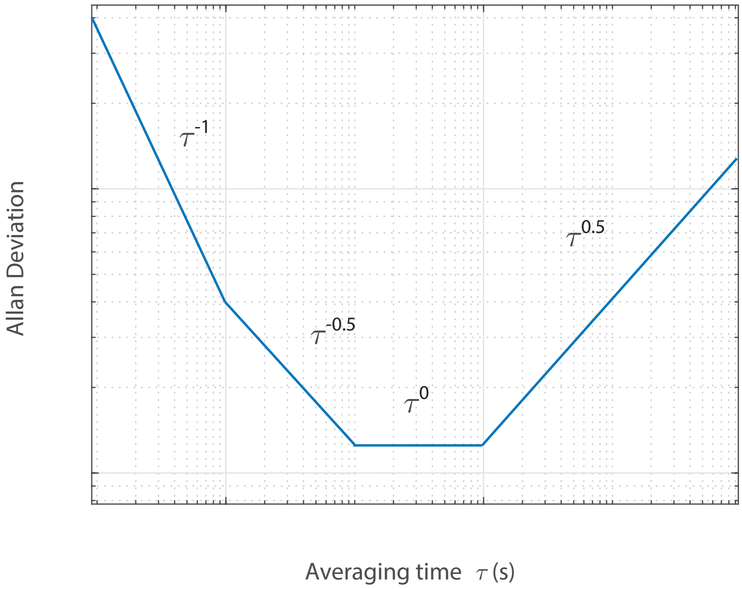

Figure 1.4: Drawing of the typical slopes of an Allan Deviation plot. Each slope represents a certain type of noise. τ^{-1} is the result of white or flicker noise in the phase of the signal. $\tau^{-0.5}$ is caused by white noise in the frequency. τ^{0} represents flicker noise in frequency. $\tau^{0.5}$ is the result of random walk, commonly caused by temperature differences, or aging of the device.

The values of $\bar{y}$ in eq. (1.3) are the averaged fractional frequency deviation over averaging time τ. Mathematically this is defined as

$$\bar{y}_k(\tau) = \frac{1}{\tau}\int_{k\tau}^{(k+1)\tau} y(t)dt \tag{1.7}$$

For discrete samples, spaced by τ_0 time and assuming $\tau = n\tau_0$ with $n = 1, 2, 3..N/2$, eq. (1.7) can be written as eq. (1.8).

$$\bar{y}_k(n\tau_0) = \frac{1}{n}\sum_{i=1+n(k-1)}^{nk} y(i\tau_0) \tag{1.8}$$

Typically, the Allan Deviation is plotted against the averaging time τ so it becomes visible for what averaging times the frequency stability is the best, i.e. the Allan Deviation is the smallest. Different types of noise in the system manifests themselves in the Allan Deviation plot [19, 20]. This relation is usually visible in the slopes of a σ_y against τ plot with logarithmic axes, see fig. 1.4. In practice, the Allan Deviation for small averaging times is limited by white frequency noise. One noise source of this type is thermomechanical noise. This is noise caused by movement of atoms in the resonator under influence of temperature bigger than absolute zero. It is known that thermomechanical noise manifests as a $\tau^{-0.5}$ slope in the Allan Deviation. Typically, at some point the slope becomes horizontal. In this region (or point), the frequency stability is the best. For longer averaging times the Allan deviation starts to increase again due to noise sources that act on a long timescale, like temperature changes or wear of the resonator.

1.3. PLL control

In the beginning of this chapter, it is stated that it is beneficial to use control if one wants to exploit the nonlinear dynamics of a resonator. As shown in section 1.1.2 and fig. 1.3, amplitude jumps occur naturally in the bistable regime. When tracking the frequency around the resonance peak, this is an issue because when the amplitude jumps down, one has to reduce the frequency to jump up and then increase the frequency again to get to the peak. Using a proper control mechanisms, jumps can be prevented.

The phenomenon of the jumps in amplitude and the procedure to get back to the peak as just described

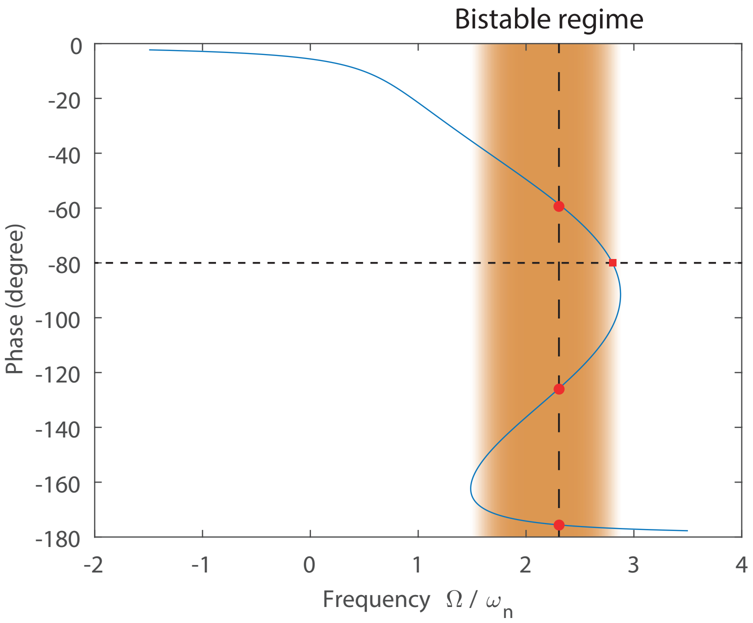

Figure 1.5: Phase response of a nonlinear resonator. The bistable regime is indicated by the coloured area. In this bistable regime, the phase is a multivalued function of the frequency. This can be seen by the vertical dashed line. At that frequency, there are three possible values for the phase, denoted by the red dots. On the other hand, the frequency is a single-valued function of the phase. The horizontal dashed line shows this, as there is only one frequency value corresponding to this phase as is indicated by the red square.

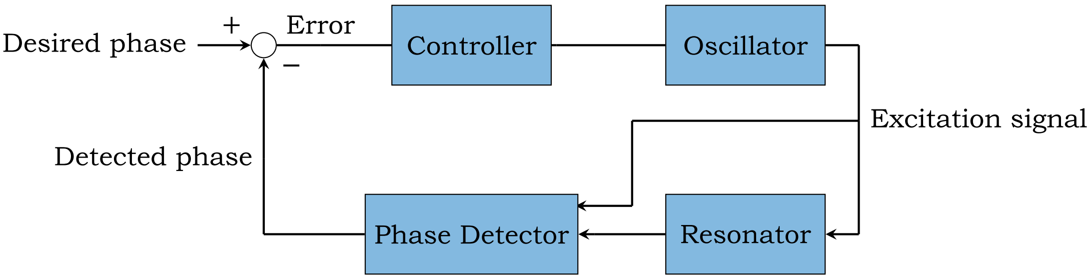

Figure 1.6: Schematic representation of a PLL. The oscillator generates the excitation signal at a certain frequency. This signal drives the resonator and goes to the phase detector. The phase detector finds the difference n phase between the signal from the oscillator and resonator. Next, the difference between the detected phase and the desired phase, called the error, is calculated. Then, the controller calculates the change in frequency that is required for a given error and the oscillator will adapt its frequency.

is also known as operation in *open loop*. This is opposed to *closed loop*, where the controller uses the output of the resonator to calculate the next input and therefore creating a loop [21]. When the output of the resonator is used to calculate a new input, this is called feedback. What information is used as feedback depends on the goal of the controller and the dynamic behaviour of the resonator. In case of a nonlinear resonator, it is beneficial to use the phase as feedback. Figure 1.5 presents the reason for this. In the bistable regime there are multiple phase values for a single frequency, but for any phase, there is only one corresponding frequency value. Therefore, using the phase as feedback, the controller can simply compare the phase of the resonator with the desired one and adjust the frequency accordingly.

A control method that uses phase feedback is the phase-locked loop (PLL). It consists of a voltage controlled oscillator (VCO), phase detector (PD) and loop filter (commonly a PI controller), see fig. 1.6. The VCO generates the exitation signal for the resonator, whose output is compared to the signal of the VCO in the phase detector. The PD yields the phase difference between these signals which then is compared to the desired phase. The loop filter acts on the difference between the desired and the actual phase. The resulting signal affects the VCO to correct its frequency to match the desired phase. A downside is that a PD typically adds delay to the loop and can limit the speed at which the PLL can correct for sudden changes. Whether a PLL can indeed stabilize the unstable branch of the nonlinear resonator depends partly on the controller. Commonly a controller with proportional and integrator gain (PI controller) is used. The P and I parameters need to be selected in such way that it stabilizes the unstable branch.

2

Paper: Frequency stability of graphene nonlinear resonators

The main findings of this thesis are presented in a scientific paper format on the next pages. The thesis itself contains lots of additional information to support the paper and experiments that were conducted but not relevant to the main findings.

Frequency stability of graphene nonlinear resonators*

Ties J.A. Verschuren[a]

[a] Dynamics of Micro and Nano Systems, Department of Precision and Microsystems Engineering, Delft University of Technology, The Netherlands

ARTICLE INFO

Keywords:
Graphene
Frequency Stability
Nonlinear resonator
Allan Deviation
Phase-locked loop
Nonlinear damping

ABSTRACT

In pursuit of extremely sensitive sensors, the dimensions of these devices get smaller and smaller. Small scale resonators are commonly used as sensors by relating changes in the dynamic behaviour to a sensed quantity. Conventionally, the dynamics used for sensing are in the linear regime. However, at smaller scales the dynamic range of the linear regime decreases. Therefore, it is of interest to investigate the dynamic behaviour in the nonlinear regime, as with the decreasing scale of the resonators this becomes inevitable. Especially, little is known about the frequency stability in this region. The frequency stability provides an indication for the potential sensitivity that the resonator can have as sensor. By using phase locked loop (PLL) the frequency stability around the resonance frequency of nonlinear resonators can be obtained. This research contains attempts to control multilayer graphene drums around its fundamental resonance frequency with PLL. In addition, the frequency stability at these points are presented by measure of the Allan Deviation. It is found that the frequency stability is the best within the bistable regime. One resonator shows behaviour attributed to internal resonance. This internal resonance is linked to an increase of nonlinear damping. Combining that with a single degree of freedom simulation model, a relation was found between increased nonlinear damping and an improvement of frequency stability.

1. Introduction

It was more than 15 years ago when graphene as 2D material was discovered [1]. Since then, a lot of research has been conducted on this new material and, among others, outstanding mechanical properties were discovered [2]. These properties make graphene a huge potential material for sensitive sensors, to sense small quantities of mass, pressure, strain, force or charge [3]. To achieve high sensitivity, it is beneficial to have a sensor that is small itself. Especially for resonant sensors where sensitivity increases with a decrease of sensor mass [3]. The sensitivity of a resonant sensor is limited by the measurement uncertainty of the resonance frequency [4]. This frequency stability can be quantified with the Allan Deviation [5].

In devices at this micro- and nanoscale, nonlinear dynamic behaviour is observed. Therefore, one needs to understand this behaviour in order to avoid or exploit it [6, 7]. Exploiting these nonlinear dynamics has become more of interest the last years to find the practical limits of sensor performance. Furthermore, an understanding of these nonlinear phenomena could potentially improve the performance beyond what was conventionally considered possible [8].

This research focusses on the nonlinear behaviour using a multilayer graphene resonator. Lasers are used to actuate and measure the displacement of the graphene. To exploit the nonlinear behaviour, the drum is controlled with a phase-locked loop (PLL). A PLL can stabilize the unstable branch of a Duffing resonator because it uses the phase as feedback and the excitation frequency is a single-valued function of the phase [9]. However, in practise it is a challenge to stabilize the unstable branch of graphene resonators because of the relatively high resonance frequencies and low Q-factors. Section 3.2 presents how this challenge can be overcome.

For sensing applications the frequency stability is of interest as this provides a lower limit on the sensitivity of resonant sensors [10]. The frequency stability of graphene resonators is an underexposed topic. The frequency stability around the resonance frequency at different phase setpoints using a PLL are presented in section 4.

The Allan Deviation, used as frequency stability measure, has not the same distribution over the frequency response for different resonators. By taking a closer look at the frequency response, the vicinity of internal resonance is predicted for one graphene drum. Using a simulation model and recent work connecting an increase of nonlinear damping to internal resonance [11], this research relates an increase of nonlinear damping to an improvement in frequency stability.

2. Experimental setup

The multilayer graphene drums are fabricated by stamping a thin flake of graphite onto a cavity etched in a layer of SiO_2 on Si [12] with a depth of 285 nm (see fig. 1). The drums have a diameter of 10 μm.

The dynamic behaviour of the graphene drum is captured by an Fabry-Pérot optical interferometer, which is schematically shown in fig. 2. A red He-Ne laser with a wavelength $\lambda = 632$ nm is used to measure the out of plane movements of the drum. The reflectivity of the light changes with position of the drum membrane and is therefore a measure for the position of the membrane [13]. The forced vibrations of the membrane are induced by a power modulated blue laser ($\lambda = 488$ nm), which acts as a thermomechanical actuator. The drum is glued in a vacuum chamber and pumped down to a pressure of 1×10^{-4} mbar.

To aim the laser at the drum, a manual positioning stage

---

* This paper is part of the authors master thesis of the same name under supervision of Ata Keşkekler and Farbod Alijani. The author gratefully acknowledges the supervisors for their guidance and Tomás Manzaneque, Irek Rosłoń and Richard Norte for helpful discussions and practical tips.

ORCID(s): `0000-0001-9756-0968` (T.J.A. Verschuren)

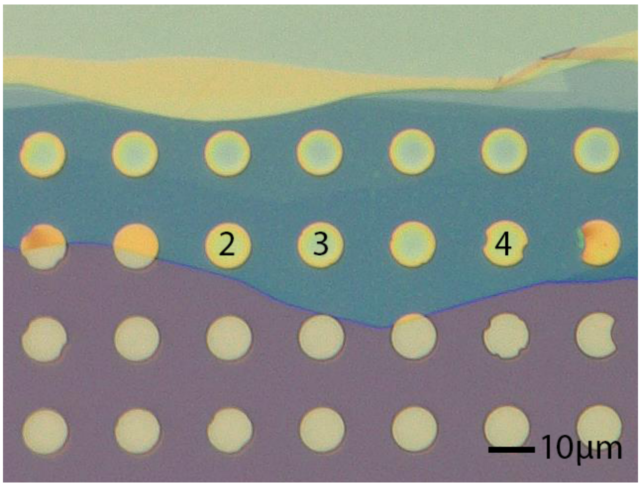

Figure 1: Image of a few drums on a SiO_2 chip made with an optical microscope (magnification 1000X). The holes have an diameter of 10 µm. The drums marked with 2, 3 and 4 are referred to as drum 2, drum 3 and drum 4 in this work.

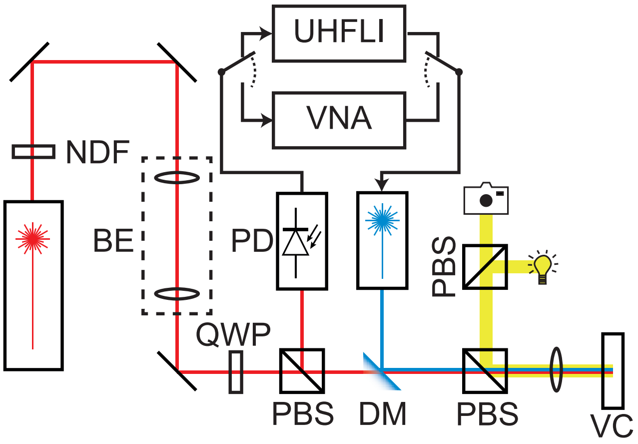

Figure 2: Schematic drawing of the Fabry-Pérot interferometer. The red laser power is controlled by a variable neutral density filter (NDF) and led through a beam expander (BE). Followed by a quarter wave plate (QWP), a couple of polarized beam splitters (PBS) and a lens. The drum is located in the vacuum chamber (VC) and the red laser is reflected back to the photodiode (PD). The blue laser is brought into the red lasers path by the dichroic mirror (DM). The photodiode is connected to the UHFLI or VNA which controls the blue laser. Images from the camera are used to position the drum and vacuum chamber. For these images a white light source is used.

is used. A camera and corresponding white light source is acting as microscope to help visually aim the lasers. By inspecting the forced frequency response of the drum, displayed by a Vector Network Analyser (VNA), the drum is positioned in such a way that the fundamental resonance peak has the highest possible amplitude [14]. To control the drum, the lasers are connected to a Zurich Instruments UHFLI (Ultra High Frequency Lock-In) which is configured as PLL.

3. Control of graphene resonator by PLL

To track the resonance frequency and overcome the amplitude jumps in the bistable region, a controller is employed. The time required by the resonator to adapt to changed external conditions is of the order $\tau \sim 2Q/\omega_0$. As graphene resonators have low Q-factors (between 100 and 600) and high resonance frequencies (1 MHz and higher) [14], it is a challenge to get the controller to respond on time. A fast control system is required, i.e. a high control bandwidth.

The use of the phase for control is beneficial, because the forcing frequency is a single-valued function of the phase. This is in contrast with the amplitude and frequency which are multivalued functions of each other. A PLL can stabilize the unstable branch of the fundamental resonance of a resonator described by the Duffing equation [9, 15].

A typical PLL consists of an oscillator, phase detector and a controller, see fig. 3. An oscillatory signal is created by the (voltage controlled) oscillator, which drives the resonator. The response of the resonator is then compared to the oscillator output in the phase detector. The phase detector can be seen as a demodulator using homodyne detection. The output is proportional to the phase difference between the signals. Next, the detected phase ($\hat{\phi}$) is compared to the phase setpoint (ϕ_c). The difference is the error e which is converted to a correction on the oscillator frequency (y). The PLL tries to minimize the error to ensure that the resonator is driven at the desired phase.

3.1. Control parameter selection

Besides an oscillator and phase detector, a PLL typically contains a PI controller. The selected proportional k_p and integrator gain k_i should stabilize the resonator for all phase values around resonance.

One way to select these parameters is by analysing the stability of PLL and resonator combined using the method of averaging [9, 15]. However, for the investigated graphene drums this method did not result in parameter values that stabilized the unstable branch. This may be caused by the usage of a perturbation method, as these methods assume small nonlinearities and forces compared to the other parameters.

Another method finds is origin in a somewhat unexpected field of study. While this paper investigates a nonlinear resonator, literature for controlling a linear resonator with PLL is consulted as this could provide values for the control parameters. In the supplementary material of [16], the next values are suggested.

$$k_p = \omega_{pll}, \qquad k_i = \frac{k_p}{\tau_c} \tag{1}$$

The desired loop bandwidth of the PLL and time constant of the resonator are denoted by ω_{pll} and $\tau_c = \frac{2Q}{\omega_0}$ respectively. The use of a linear model makes it therefore easy to select and investigate the loop bandwidth of the PLL [17]. However, when using a graphene nonlinear resonator, k_p loses its meaning.

Next to k_p and k_i, a value needs to be selected for the demodulation filter cut-off frequency ω_c in the phase detector.

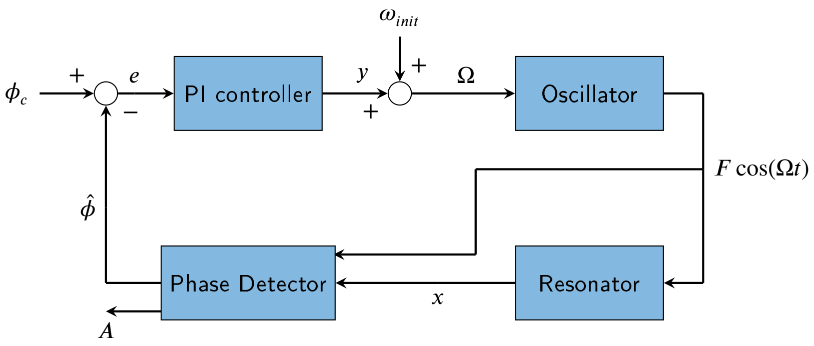

Figure 3: Schematic representation of a resonator incorporated with a PLL. The oscillator generates a periodic signal with frequency Ω and amplitude F to drive the resonator. In the phase detector the response of the resonator is compared with the driving signal resulting in the estimated phase difference $\hat{\phi}$. This phase is then compared to the phase set-point ϕ_c and on this difference, the error, acts a PI controller. The resulting correction y of the controller is added to the initial driving frequency ω_{init} and proceeds as the oscillator frequency Ω.

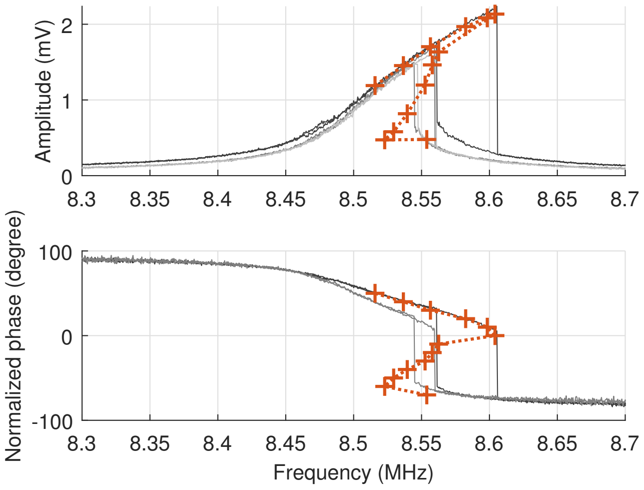

Figure 4: Amplitude and phase response around the first mode of drum 1 while being controlled by PLL. The controlled points are denoted by the blue markers. A line is drawn between them to compare with the sweeps. The grey lines are forward and backward sweeps of the drum taken before, during and after the experiment. Clearly the response changes over time, presumably due to slight movement of the positioner.

As a rule of thumb, the following applies: $\omega_0 >> \omega_c >> \omega_{pll}$. Distinguishing a factor 10 between the natural resonance, demodulator cut-off and loop bandwidth frequency works in practise.

3.2. Stabilize the unstable branch

To control the drum, the lasers are connected to a Zurich Instruments UHFLI which is configured as a PLL. Before doing the experiment, the driving power is decreased until the frequency response of the drum is linear and can be used to fit the resonance frequency $f_0 = \omega_0/(2\pi)$ and Q-factor with the UHFLI. These values are used to calculate k_i. After converting the k_p and k_i to match the UHFLI parameter units, the demodulator filter cut-off frequency is set to $f_c \approx f_0/10$. With the PLL enabled, the phase setpoint is swept to recreate the frequency response curve of the graphene resonator.

The procedure described above is applied to drum 1. The extracted values are $f_0 = 8.495$ MHz and $Q = 295$. These parameters are fitted while using a blue laser power of −5 dBm. Later experiments use a power of 5 dBm. A 4th order demodulator low pass filter is set to $f_c = 100$ kHz and $f_{pll} = \omega_{pll}/(2\pi) = 10$ kHz, resulting in $k_p = -174.5$ and $k_i = -2.958 \times 10^4$. These values do not work well for phase setpoints close to resonance peak and therefore the linear PLL bandwidth was increased $f_{pll} = 100$ kHz. Likewise, the demodulator low pass filter cut-off frequency was raised to the maximal value possible $f_c = 674.8$ kHz and k_p and k_i are increased accordingly.

With these values the PLL is able to control the drum, although the standard deviation on the error signal σ_e grows on the unstable branch, from 10° to 80°. The phase setpoint is swept with steps of 10° over the course of five hours. Before, during and after the measurements an open loop frequency sweep is performed. Figure 4 indicates that it is possible to control the unstable branch of the graphene resonator. The figure also reveals that the open loop sweep changes over time. Most likely this is caused by tension in the connection of the vacuum chamber to the pump causing the positioner to move a little over time. In this research, only the unstable branch of drum 1 was successfully stabilized. In other experiments only the stable branches of the resonance peak were investigated.

4. Frequency stability

When using a resonator for sensing, the frequency stability is a property of interest. For resonant sensors, the frequency stability limits the minimal sensitivity of the sensor [4, 18]. For graphene nonlinear resonators it is not known where at the resonance curve the frequency stability is optimal. Therefore, the frequency stability of graphene resonators is investigated. In this paper, the 2-sample Allan Deviation is used. This deviation is a function of the aver-

Table 1
Parameter values for eq. (2) found by comparing the frequency response of the Duffing equation with the open loop frequency sweep of drum 4.

Parameter	Value
b	0.0057
η	980
γ	9100
F	6×10^{-5}

aging time τ [5]. The Allan Deviation is typically presented in a log-log plot where different noise types in the resonator and actuation and measurement system can be distinguished by their slope. This slope can be described by the value of α in the function τ^{α}. Characteristic is the slope for $\alpha = -0.5$, as this indicates white noise in the frequency, since this is the primary disturbance of frequency stability. For sensor applications one is interested in the lowest Allan Deviation because this corresponds with the best frequency stability and therefore the best sensitivity. The corresponding averaging time is also of interest, as the application can require a certain averaging time.

In this research, data is collected while the drum is controlled by the PLL to determine the Allan Deviation for a graphene resonator. For each phase setpoint on the stable branch of the resonance peak, the demodulator frequency, phase and amplitude are recorded for 2 min at a sampling rate of 100 kHz. From the recorded frequency data the Allan deviation can be calculated. The phase and amplitude data is used to recreate the frequency response.

4.1. Frequency stability for different phase setpoints

The procedure described above is applied to three different graphene resonators: drum 2, drum 3 and drum 4. In fig. 5a the Allan Deviation for drum 2 is presented. From the figure it becomes clear that for lower averaging times the frequency stability is limited by white frequency noise, indicated by the $\tau^{-0.5}$ slope. After reaching a minimum value, the Allan Deviation increases again. However, this plot does not clearly show how the frequency stability changes with the PLL setpoint. For this reason the minimal Allan Deviation for each PLL setpoint is plotted with the open loop frequency sweep of the different drums in figs. 5b to 5d. It stands out that figs. 5b and 5d reveal a minimal Allan Deviation within the bistable region. However, fig. 5c shows that this point is at the resonance peak.

5. Simulations

A simulation model is built in attempt to explain the behaviour found in the previous section. The PLL is modelled with MATLAB Simulink[1] after the control loop in fig. 3. The oscillator is imposed by an integrator followed by a cosine block and a constant gain F. This results in an oscillatory output signal with amplitude F and frequency Ω. The phase detector employs homodyne detection and synchronous demodulation to find the phase difference between the two signals [19, 20]. The two outputs are proportional to the phase and amplitude of the resonator output. White noise with power S_{TMN} is added to the input signal of the resonator to represent the thermomechanical noise. It is added to the force instead of the phase signal because amplitude-phase noise conversion occurs in nonlinear resonators [21]. Additionally, white noise with power S_A is added to the resonator output to mimic the noise floor from the measurements. The Allan Deviation is calculated from the oscillator frequency Ω. This signal is decimated to match the 100 kHz sampling frequency from the experiments.

As a model for fundamental resonance of the graphene resonator, the Duffing equation is used. Fitting this equation to the open loop frequency response of drum 4 results in the following mass and resonance frequency normalized Duffing equation:

$$\ddot{x} + b\dot{x} + \eta\dot{x}x^2 + x + \gamma x^3 = F\cos(\Omega t) \tag{2}$$

The parameters b, η, γ, F and Ω are linear damping, nonlinear damping, cubic stiffness, amplitude of the driving force and frequency of the driving force respectively. Values for these parameters are found by assuming $b = 1/Q$ and tuning the other values while comparing the frequency response of the model with the open loop frequency response of drum 4. The frequency response of the model is created with AUTO 97 [22]. The resulting values are presented in table 1. Now the noise powers can be defined. The thermomechanical noise power is described by:

$$S_{TMN} = 4k_bTb \tag{3}$$

where k_b, T and b are the Boltzmann constant, temperature in Kelvin and the coefficient of damping of the drum, respectively [23]. When assuming $T = 300\,\mathrm{K}$, it follows that $S_{TMN} = 9.47 \times 10^{-23}\,\mathrm{N^2\,Hz^{-1}}$. S_A is set to $1.8924 \times 10^{-5}\,\mathrm{V^2\,Hz^{-1}}$, as this is the average noise floor coming from the measurements. Due to the large difference between the noise powers, it is expected that the influence of thermomechanical noise is not visible at all. This corresponds with the experiments where it was impossible to present a clear thermomechanical peak.

Simulations are executed for $t_s = 1 \times 10^6$ (normalized time). When calculating the Allan Deviation, the first 1×10^5 s simulation time is discarded as this time is required to reach steady state. The resulting Allan Deviation is compared with the experimental one in fig. 6. The simulation and experimental acquired values do not match. The best frequency stability was reached at 60° for the simulations and 45° for the experiments.

Despite the simulation mismatch, the simulations will be used to show another phenomenon later in this paper.

---

[1] MATLAB 2019b, copyright The MathWorks, Inc.

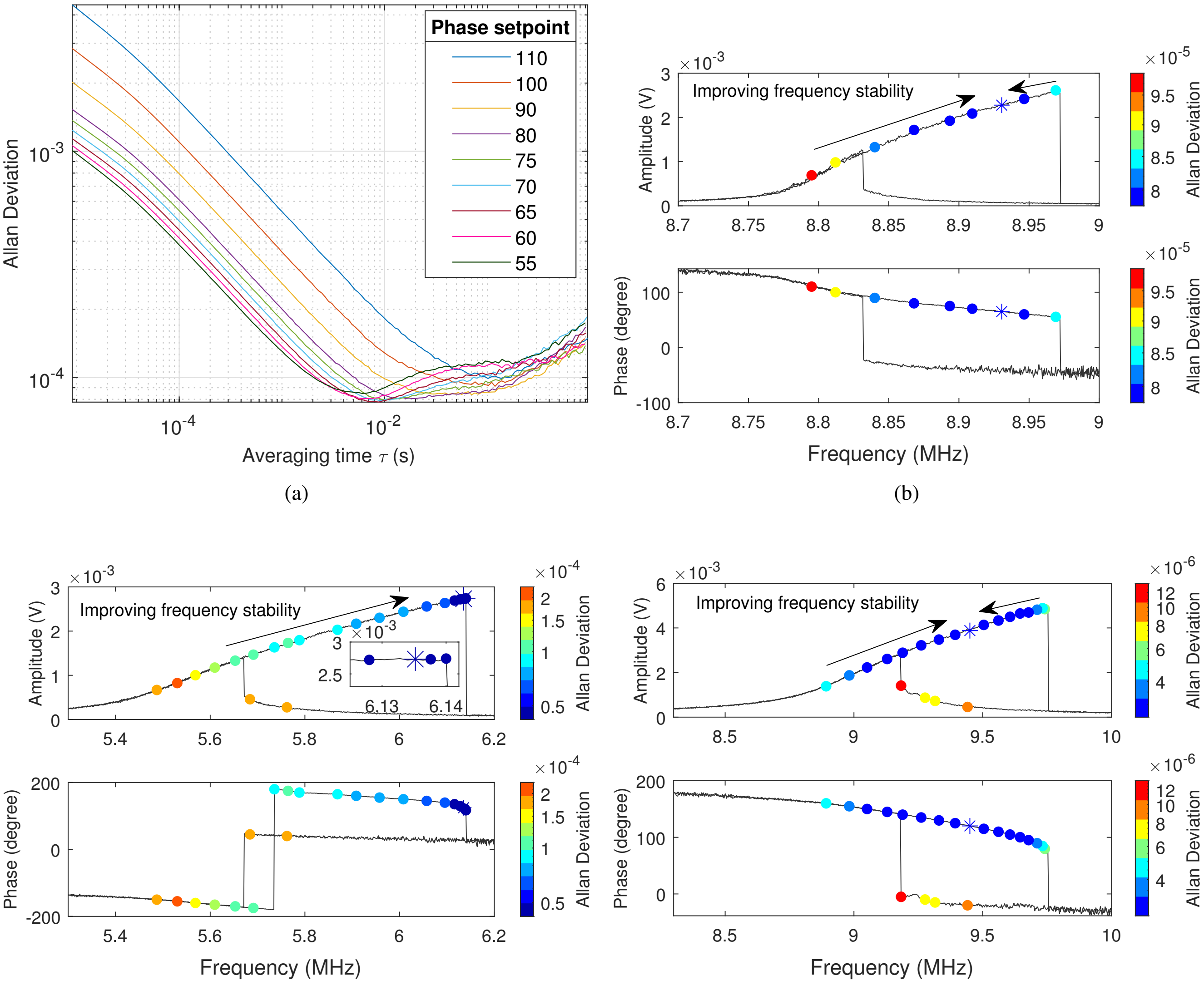

(a)

(b)

(c)

(d)

Figure 5: (a) Allan Deviation for the stable branch of drum 2 while controlled by PLL. For small averaging times, the frequency stability is limited by white frequency noise. This is indicated by the $\tau^{-0.5}$ slope. For the different phase setpoints the minimal Allan Deviation is different. **(b)**, **(c)** and **(c)** Open loop frequency response with the dots indicating the minimal Allan deviation during PLL control at that setpoint for drum 2, drum 3 and drum 4 respectively. The star indicates the lowest Allan Deviation and therefore the best frequency stability. The more dark blue the better the frequency stability.

5.1. Influence of nonlinear damping on frequency stability

Next, the dynamic response of drum 3 is inspected more closely. Figure 7 shows the open loop frequency sweeps of this drum for different excitation levels. It stands out that the descending difference of drop down frequencies for successive excitation levels. This suggests an increase in nonlinear damping. Recent work shows that nonlinear damping in graphene resonators increases as much as by 80 % when operated near internal resonance [11]. This raises the question if the frequency stability is influenced by a changing nonlinear damping.

To investigate this, the simulation model with the same parameter values from table 1 is used. The nonlinear damping parameter η is set to $980\,\mathrm{N\,s\,m^{-3}}$ and $9800\,\mathrm{N\,s\,m^{-3}}$. The Allan Deviation for different phase setpoints is calculated in both cases and compared in fig. 8. From this figure it is clear that for all the phase setpoints the frequency stability improved with an increase of the nonlinear damping. The best frequency stability setpoint has moved from 60° to 80°. Therefore, the increase in nonlinear damping also explains the difference in the position of the best frequency stability point in fig. 5c compared to figs. 5b and 5d.

6. Discussion & Conclusion

As presented in the literature [9, 15] and fig. 4, it is possible to fully control a nonlinear resonator with a PLL. However, the challenge exists in finding proper control parameters. Although multiple analyses exist, they seem not al-

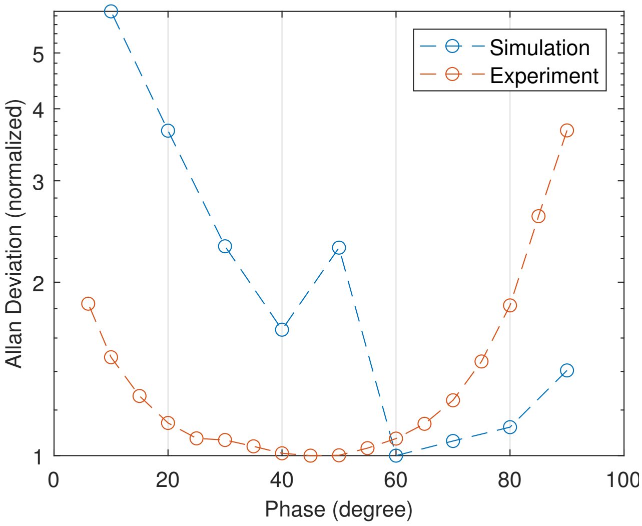

Figure 6: Comparison of the Allan Deviation per PLL setpoint between the simulations and the experimental measured values of drum 4. The phase is normalized so the resonance peak is at 90°.

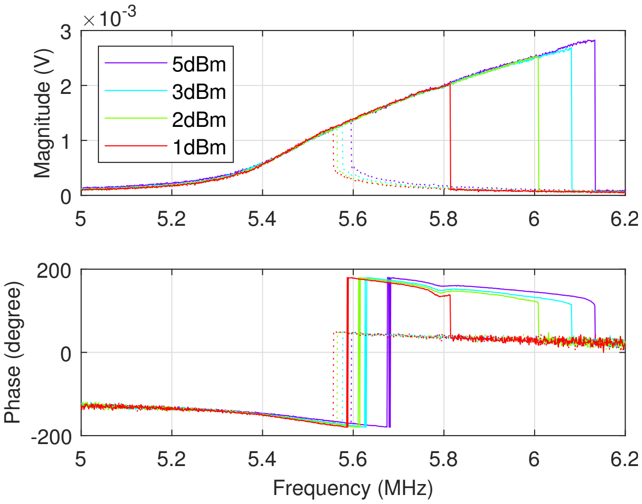

Figure 7: Open loop frequency sweeps for different powers of drum 3. The dotted lines are the corresponding backward sweeps. The difference between the jump down frequencies of two consecutive power levels decreases. This suggests the vicinity of internal resonance.

ways one-to-one applicable to the multilayer graphene resonators presented in this work. The method for control parameter selection assumes a linear resonator and therefore does not include stability analysis of the unstable branch. Additionally, the advantage of simple selection of the PLL bandwidth is not valid anymore when using a nonlinear resonator. Although it was possible to fully control a drum with these linear parameters, the exact PLL bandwidth is unknown. Hence, it is hard to say what bandwidth is required to control these graphene resonators.

Subsequently, the phase error standard deviation increased up to 80°, due to noise in the system. The mean phase error was approximately 0°, so over time the controller does its job. However, because of practical limits in the data acquisition equipment, the maximal sampling rate was in the 100 kHz range. Accordingly, it is not for sure that the resonator amplitude or phase quickly changes between two data points. This might be investigated by connecting an oscilloscope to the resonator output.

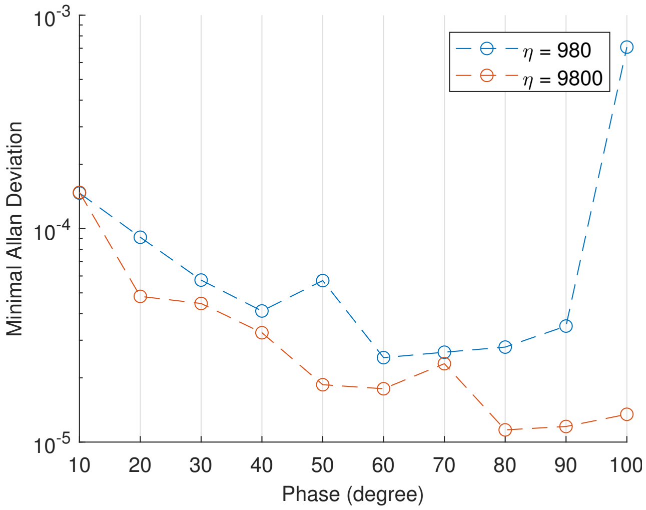

Figure 8: Allan Deviation calculated from simulations for different values of the nonlinear damping parameter η.

Although it was possible to stabilize the unstable region of drum 1, this stabilization did not succeed for drum 2, drum 3 and drum 4. Despite that all drums show nonlinear behaviour when excitation power of 5 dBm is applied, linear behaviour is observed at different power levels. The drums behave linear when the applied power is −5 dBm, −10 dBm, −20 dBm and −15 dBm for drum 1, drum 2, drum 3 and drum 4 respectively. What stands out is that drum 1 behaves linear at a relatively high power. One could speculate that the drum behaves slightly different and has a less strong nonlinearity. This may be the reason why it was possible to control drum 1 and not the others. Further research in developing better methods for selection of control parameters is needed to get more predictable results for this kind of resonators.

The presented simulation model does not match the experiments. A reason for this is the use of the normalized Duffing equation and the absence of sufficient computing time. The linear resonance frequency of drum 4 is around 9 MHz. Therefore, a simulation time $t_s = 1 \times 10^6$ would be $1 \times 10^6/(2\pi 9 \times 10^6) = 17.7$ ms in an experiment. As the experimental data is recorded for 2 min, this is a big difference. Especially since the precision Allan Deviation depends on the number of samples, running the simulation for about 6.8×10^9 could improve the result. The computational resources required for running the simulation for this time period were not available in this research.

Another improvement to the simulation is using a model that better reflects the behaviour of graphene. The Duffing equation is a single degree of freedom model, but graphene is way more complex. In this study, modal interactions and internal resonances were left out of the simulation. By including these properties in the resonator model and using sufficient computation resources, the simulation can be improved.

From fig. 8 it shows that an increased nonlinear damping has a positive effect on the frequency stability. However, this is not fully validated by the experiments conducted in this research, although drum 3 shows clearly behaviour of increased nonlinear damping in contrast to the other drums. Whether an increase in nonlinear damping will always result in the improvement of frequency stability near the resonance peak is something that requires additional attention.

In summary, this research has shown that it is possible to control a multilayer graphene resonator fully around its resonance phase. This opens a path to exploit the nonlinear behaviour of such resonators instead of avoiding it. Furthermore, the frequency stability of graphene resonators around its resonance phase is presented. Taken into account that recent work [11] discovered an increase of the nonlinear damping near internal resonance, this work relates an increase in nonlinear damping to an improvement in frequency stability. It shows that graphene resonators have the potential to be applied as sensors while operated in the nonlinear regime.

References

[1] A. K. Geim, K. S. Novoselov, The rise of graphene, Nat Mater 6 (2007) 183–91.

[2] A. Nag, A. Mitra, S. C. Mukhopadhyay, Graphene and its sensor-based applications: A review, Sensors and Actuators A: Physical 270 (2018) 177–194.

[3] Z. H. Khan, A. R. Kermany, A. Öchsner, F. Iacopi, Mechanical and electromechanical properties of graphene and their potential application in mems, Journal of Physics D: Applied Physics 50 (2017).

[4] M. Sansa, E. Sage, E. C. Bullard, M. Gély, T. Alava, E. Colinet, A. K. Naik, L. G. Villanueva, L. Duraffourg, M. L. Roukes, G. Jourdan, S. Hentz, Frequency fluctuations in silicon nanoresonators, Nature Nanotechnology 11 (2016) 552–558.

[5] F. L. Walls, D. W. Allan, Measurements of frequency stability, Proceedings of the IEEE 74 (1986) 162–168.

[6] A. Z. Hajjaj, N. Jaber, S. Ilyas, F. K. Alfosail, M. I. Younis, Linear and nonlinear dynamics of micro and nano-resonators: Review of recent advances, International Journal of Non-Linear Mechanics 119 (2020).

[7] R. Lifshitz, M. C. Cross, Nonlinear Dynamics of Nanomechanical Resonators, Wiley, 2010, pp. 221–266. doi:10.1002/9783527629374.ch8.

[8] R. Karabalin, Nonlinear and Parametric NEMS Resonators, Springer Netherlands, Dordrecht, 2015, pp. 1–13. doi:10.1007/978-94-007-6178-0_101003-1.

[9] V. Denis, M. Jossic, C. Giraud-Audine, B. Chomette, A. Renault, O. Thomas, Identification of nonlinear modes using phase-locked-loop experimental continuation and normal form, Mechanical Systems and Signal Processing 106 (2018) 430–452.

[10] F. Riehle, Frequency Standards: Basics and Applications, Frequency Standards: Basics and Applications, Wiley Blackwell, 2003. doi:10.1002/3527605991.

[11] A. Keşkekler, O. Shoshani, M. Lee, H. S. J. van der Zant, P. G. Steeneken, F. Alijani, Enhancing nonlinear damping by parametric-direct internal resonance, 2020. arXiv:2006.09364.

[12] A. Castellanos-Gomez, M. Buscema, R. Molenaar, V. Singh, L. Janssen, H. S. J. van der Zant, G. A. Steele, Deterministic transfer of two-dimensional materials by all-dry viscoelastic stamping, 2D Materials 1 (2014).

[13] D. Davidovikj, J. J. Slim, S. J. Cartamil-Bueno, H. S. van der Zant, P. G. Steeneken, W. J. Venstra, Visualizing the motion of graphene nanodrums, Nano Lett 16 (2016) 2768–73.

[14] D. Davidovikj, F. Alijani, S. J. Cartamil-Bueno, H. S. J. van der Zant, M. Amabili, P. G. Steeneken, Nonlinear dynamic characterization of two-dimensional materials, Nat Commun 8 (2017) 1253.

[15] M. Fan, M. Clark, Z. C. Feng, Implementation and stability study of phase-locked-loop nonlinear dynamic measurement systems, Communications in Nonlinear Science and Numerical Simulation 12 (2007) 1302–1315.

[16] S. Olcum, N. Cermak, S. C. Wasserman, S. R. Manalis, High-speed multiple-mode mass-sensing resolves dynamic nanoscale mass distributions, Nature Communications 6 (2015).

[17] A. Demir, M. S. Hanay, Fundamental sensitivity limitations of nanomechanical resonant sensors due to thermomechanical noise, IEEE Sensors Journal 20 (2020) 1947–1961.

[18] R. M. R. Pinto, P. Brito, V. Chu, J. P. Conde, Thin-film silicon mems for dynamic mass sensing in vacuum and air: Phase noise, allan deviation, mass sensitivity and limits of detection, Journal of Microelectromechanical Systems 28 (2019) 390–400.

[19] Zurich Instruments, Principles of lock-in detection and the state of the art, White Paper, Zurich Instruments, 2016. URL: https://www.zhinst.com/europe/resources/principles-lock-detection.

[20] D. K. Lindner, J. Twiefel, M. Klubal, C. Paiz, S. Mojrzisch, H. Krüger, Digital signal processing for an adaptive phase-locked loop controller, in: Modeling, Signal Processing, and Control for Smart Structures 2008, 2008, pp. 75 – 86. doi:10.1117/12.776091.

[21] E. Kenig, M. C. Cross, L. G. Villanueva, R. B. Karabalin, M. H. Matheny, R. Lifshitz, M. L. Roukes, Optimal operating points of oscillators using nonlinear resonators, Phys Rev E Stat Nonlin Soft Matter Phys 86 (2012) 056207.

[22] E. J. Doedel, A. R. Champneys, T. F. Fairgrieve, Y. A. Kuznetsov, B. Sandstede, X. Wang, Auto 97: Continuation and bifurcation software for ordinary differential equations (with homcont), 1998.

[23] J. C. Doll, B. L. Pruitt, Sensitivity, Noise and Resolution, 2013, pp. 51–83. doi:10.1007/978-1-4614-8517-9_3.

3

Recommendations

A goal of this thesis is to provide a foundation for further research. In this chapter recommendations and directions for further research are presented.
The recommendations are divided in three topics and presented below.

3.1. Recommendations regarding control

In general, there is a lot to learn about controlling nonlinear resonators. For this thesis, the next recommendations are made concerning control:

- Use active adaptive or nonlinear control. These methods suppress the nonlinearities in the resonator by cancelling them with the resonator input signal (Interview with Hassan HosseinNia, Assistant Professor Mechatronic System Design, Delft University of Technology. January 20, 2020).
- Apply sliding mode control. This is a method consisting of two parts. One part that tries to get close to the setpoint and another part that keeps it at the setpoint (Interview with Hassan HosseinNia, Assistant Professor Mechatronic System Design, Delft University of Technology. January 20, 2020).
- Use a more sophisticated model for graphene in simulations to test the controller. This thesis uses a single degree of freedom model, but graphene itself is way more complex. The actuation is now modelled as an external force. However, the laser is changing the tension in the drum causing it to vibrate. Downside is that this will require more computational effort.

3.2. Recommendations regarding frequency stability

The ultimate goal for sensors is to reach the frequency stability limit of the thermomechanical noise. However, as that is not the case in this thesis, the following recommendations are made.

- Explorer if and how the frequency stability changes when changing the extrication power. This is specially interesting when combined with smaller steps in the phase sweep.
- Use overlapping samples in the Allan Deviation. This increases computing power, but the uncertainty of the Allan Deviation reduces as more samples are used.

3.3. Recommendations regarding experiments

One can have a very sophisticated model and controller, but in the end it needs to work in practice. The next recommendations concern the used measurement setup and the procedure.

- Measure the dynamics of the measurement setup itself to see how it influences the measurements.

- Analyse the noise in the different components of the measurement setup to get an image of what the limiting components are for measurements of frequency stability.
- Use a nano positioner in a vacuum chamber to aim the laser at the drum and keep it that way. Manual positioners have a bad resolution and do not actually move only one axis at the time.
- Automate as much as possible. When analysing the frequency stability, it gets really tedious to wait a few minutes for each phase setpoint.
- When the process is automated, it is recommended to record data for longer times as this decreases the uncertainty of the Allan Deviation.

A

Experimental results

This chapter contains experimental results per graphene drum. The results are grouped by chip and drum coordinates related to their positions on the chip, see fig. B.1. These coordinates have the format `a_b.x.y` where `a` is the diameter of the cavity in µm, `b` is the number of the column where the drum is located (left is 1). `x` and `y` represent the horizontal and vertical number of the drum in this column and row, where the top left drum is `x`=1 and `y`=1. For example, 10_2.3.5 is a drum with a diameter of 10 µm, in the second column, the third hole from the left and the fifth one from the top.

The drums in the paper are mapped as follows:

Drum coordinates	Referred in paper by
Chip 3 10_2.5.8	drum 1
Chip 5 10_2.13.2	drum 2
Chip 5 10_2.14.2	drum 3
Chip 5 10_2.16.2	drum 4

A.1. Chip 2

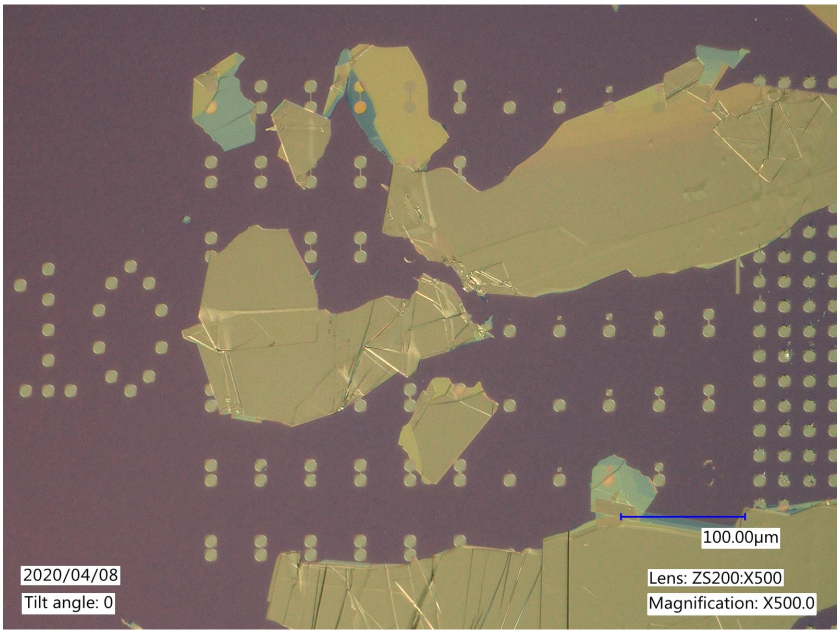

Figure A.1: Detail of chip 2 where the most interesting drums are located.

A.1.1. Drum 10_1.4.2

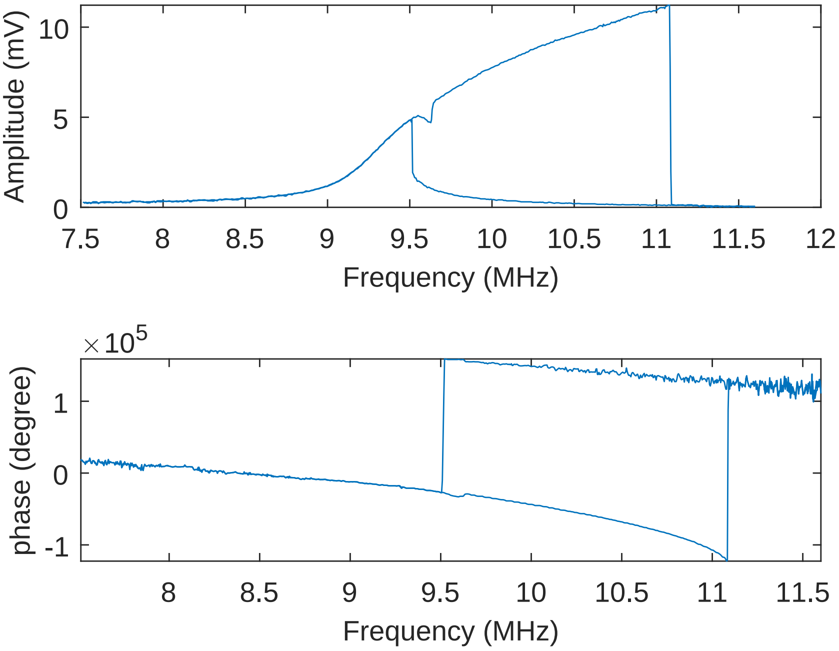

Figure A.2: Frequency response of drum 10_1.4.2 with a power of 5 dBm

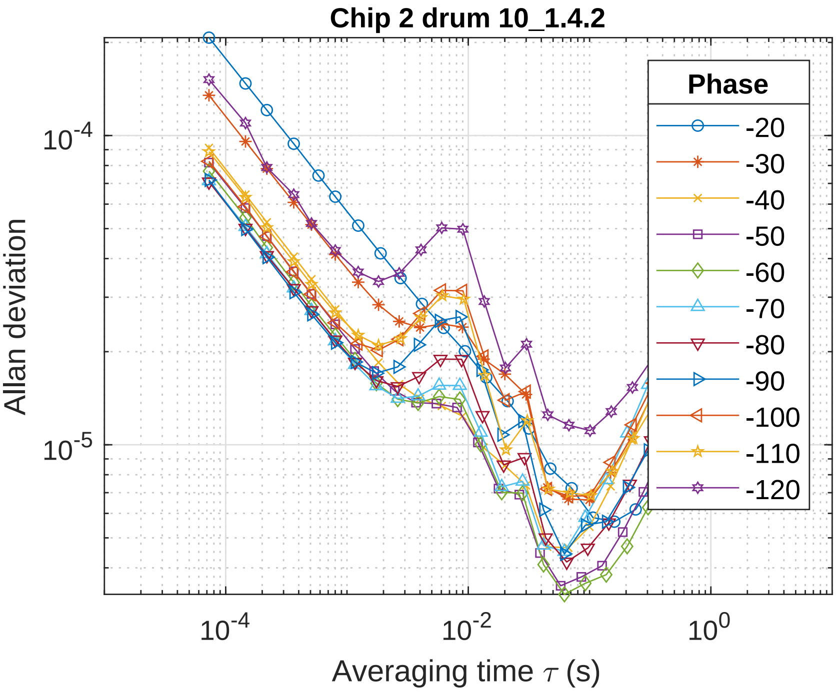

Figure A.3: Allan Deviation for drum 10_1.4.2

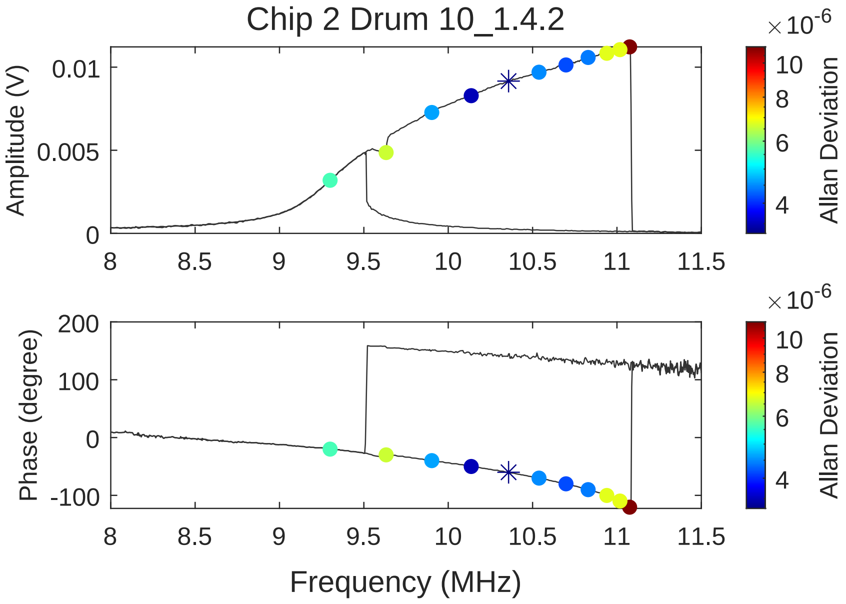

Figure A.4: Allan Deviation at the frequency response for drum 10_1.4.2

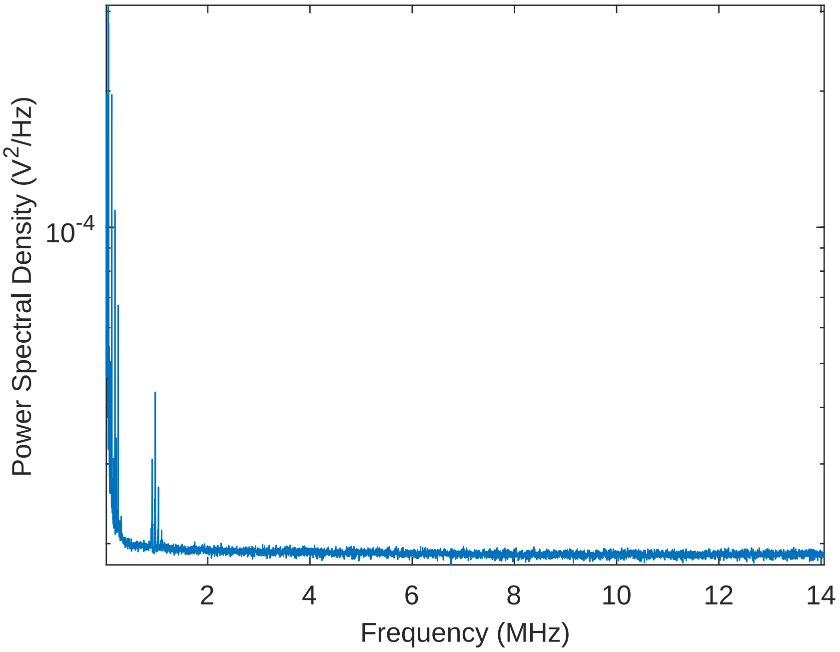

Figure A.5: Power spectrum density of drum 10_1.4.2, with the blue laser turned off. There is no thermomechanical peak visible at the resonance frequency.

A.2. Chip 3

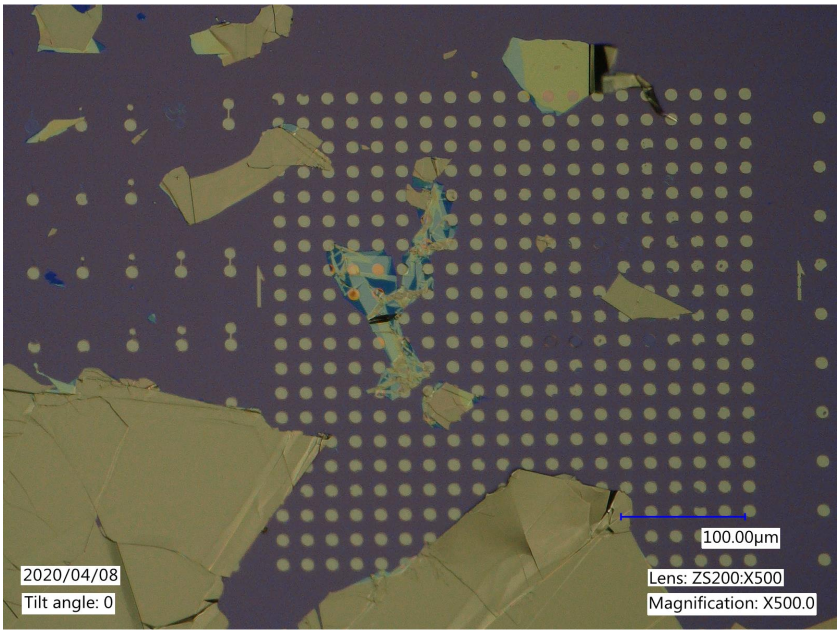

Figure A.6: Detail of chip 3 of region 10_2.

A.2.1. Drum 10_2.5.8

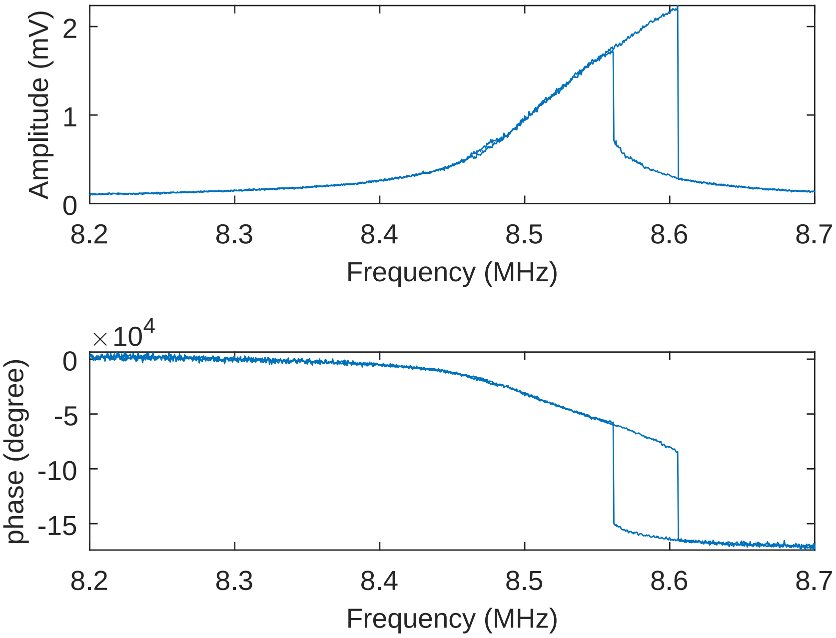

Figure A.7: Allan Deviation for drum 10_2.5.8 with a power of 5 dBm

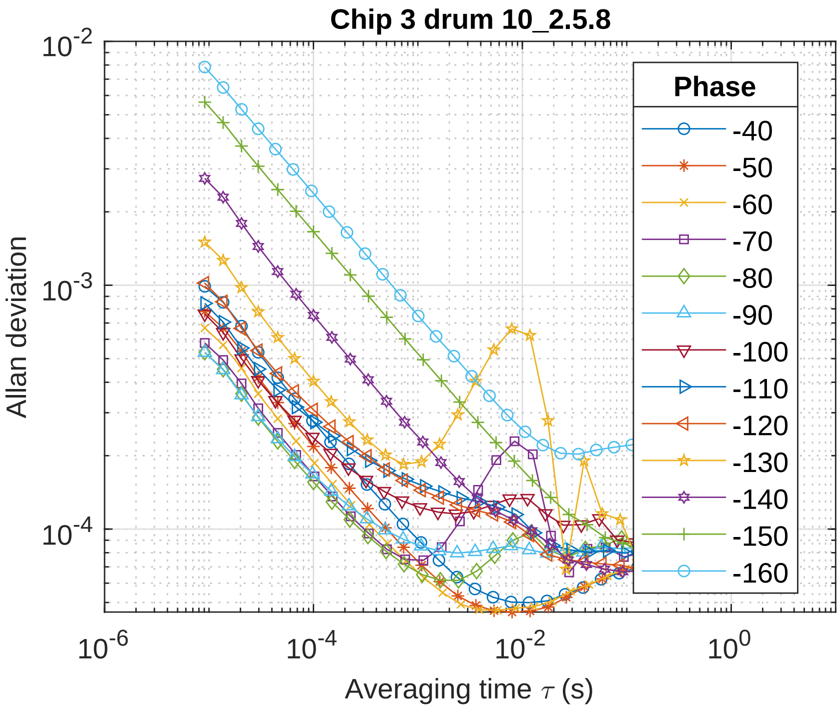

Figure A.8: Allan Deviation for drum 10_2.5.8

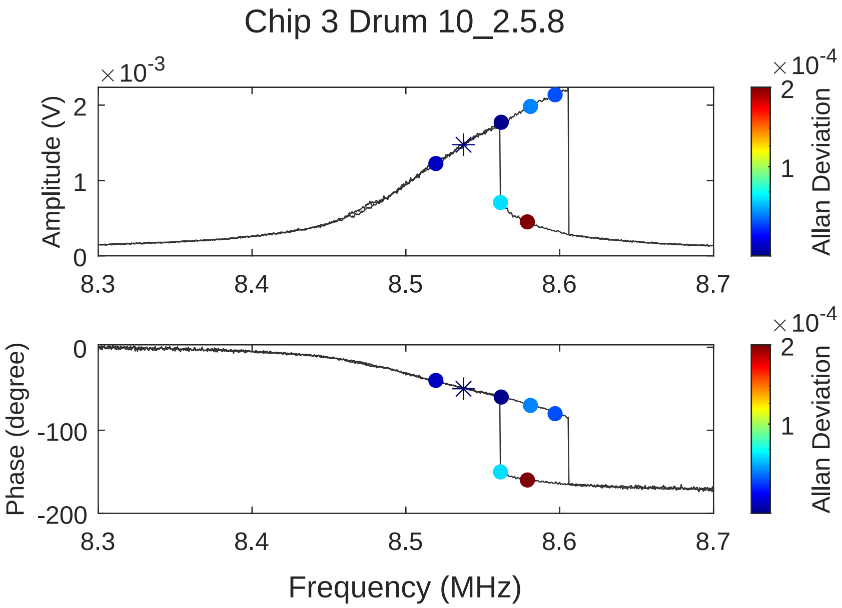

Figure A.9: Allan Deviation at the frequency response for drum 10_2.5.8

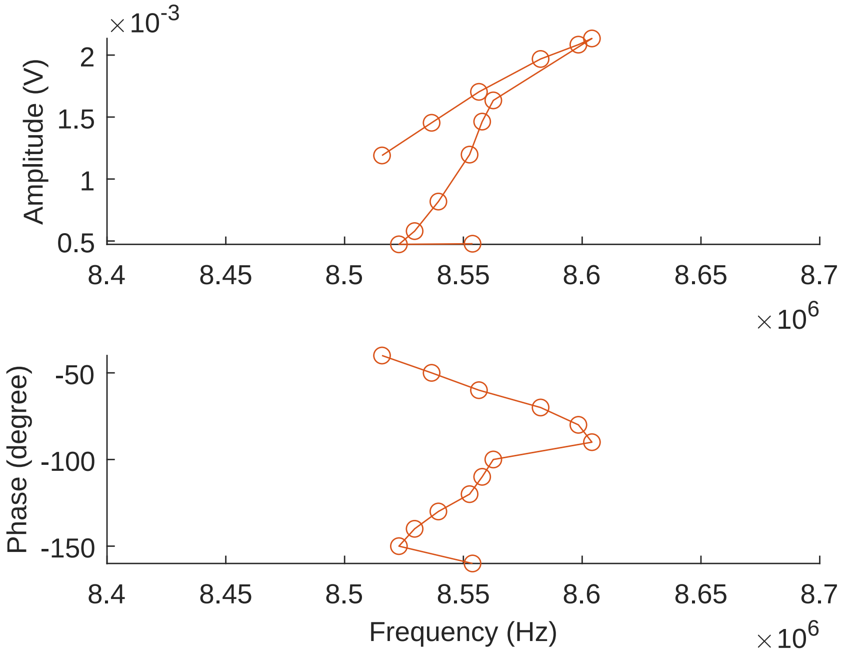

Figure A.10: The result of controlling the unstable branch of drum 10_2.5.8. The data points are acquired by averaging over 1 s of frequency, amplitude and phase data.

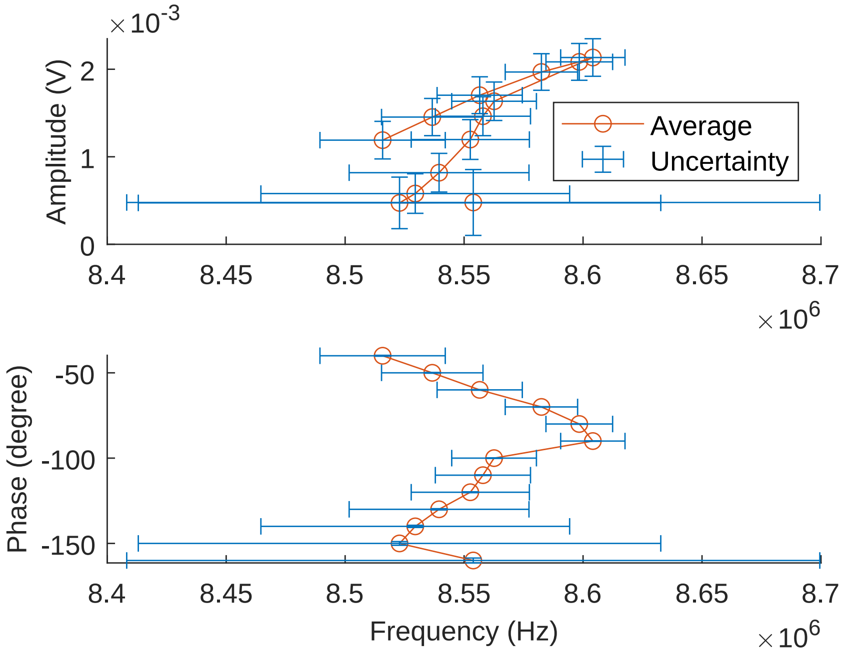

Figure A.11: The result of controlling the unstable branch of drum 10_2.5.8. The uncertainty is one standard deviation of the data, in both directions.

A.3. Chip 5

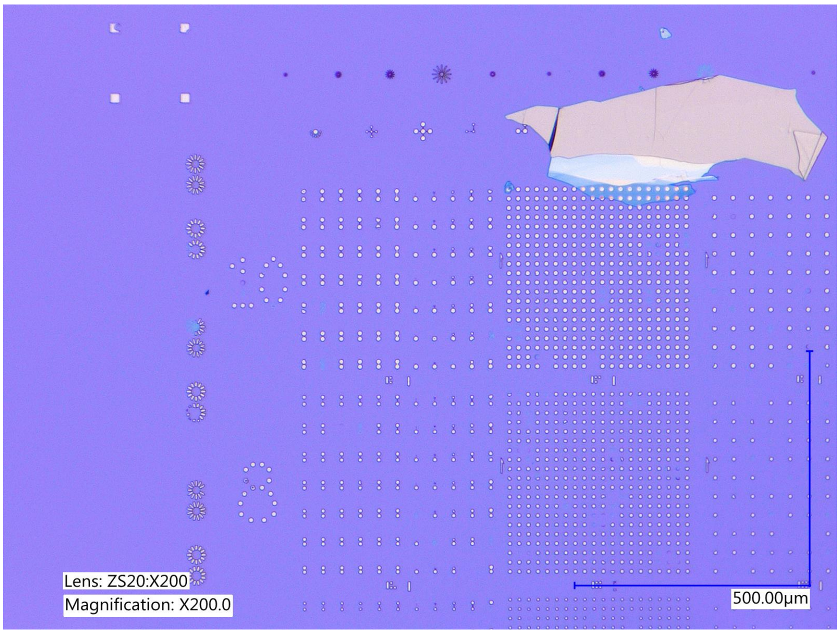

Figure A.12: Detail of chip 5 of the first two columns of 10 µm cavities.

A.3.1. Drum 10_2.13.2

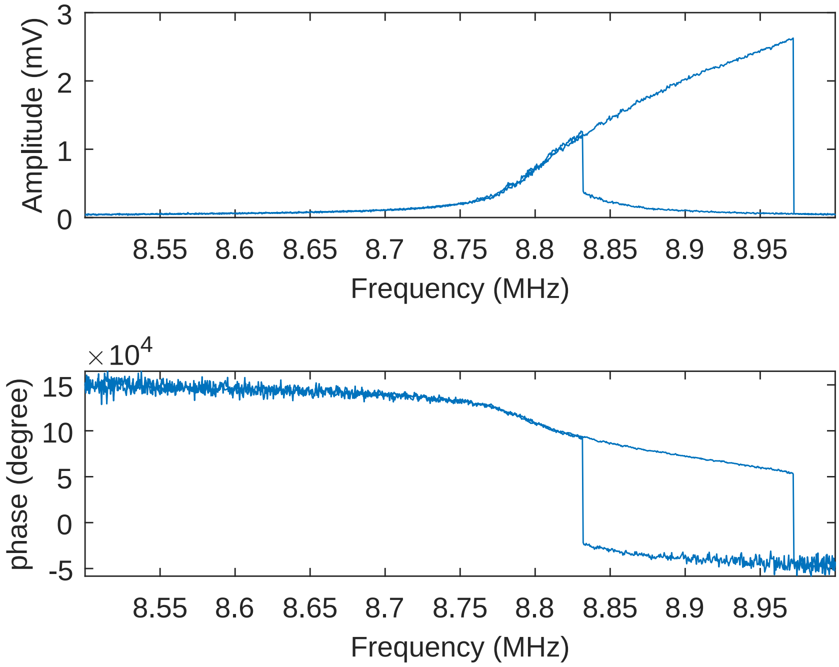

Figure A.13: Allan Deviation for drum 10_2.13.2 with a power of 5 dBm

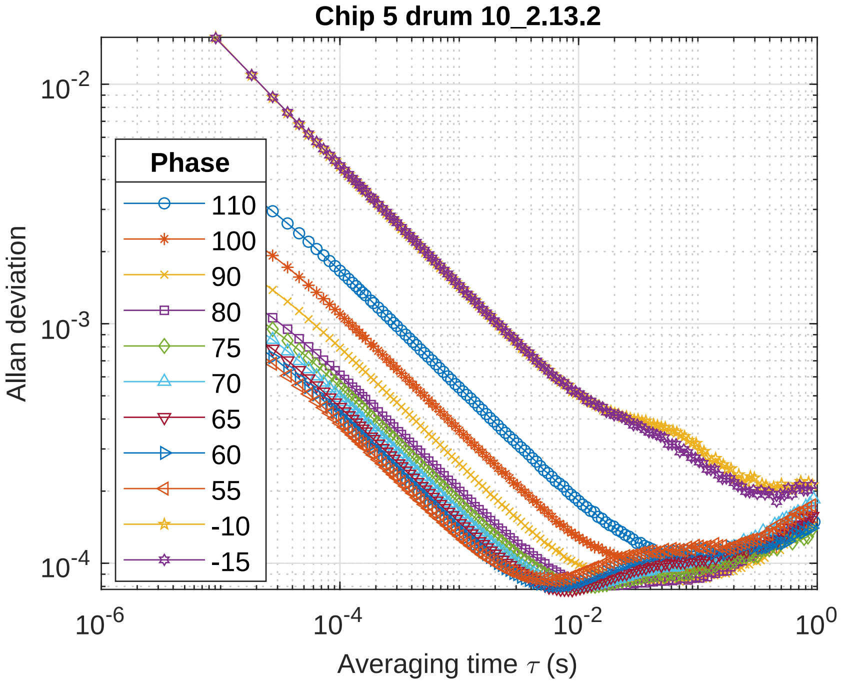

Figure A.14: Allan Deviation for drum 10_2.13.2

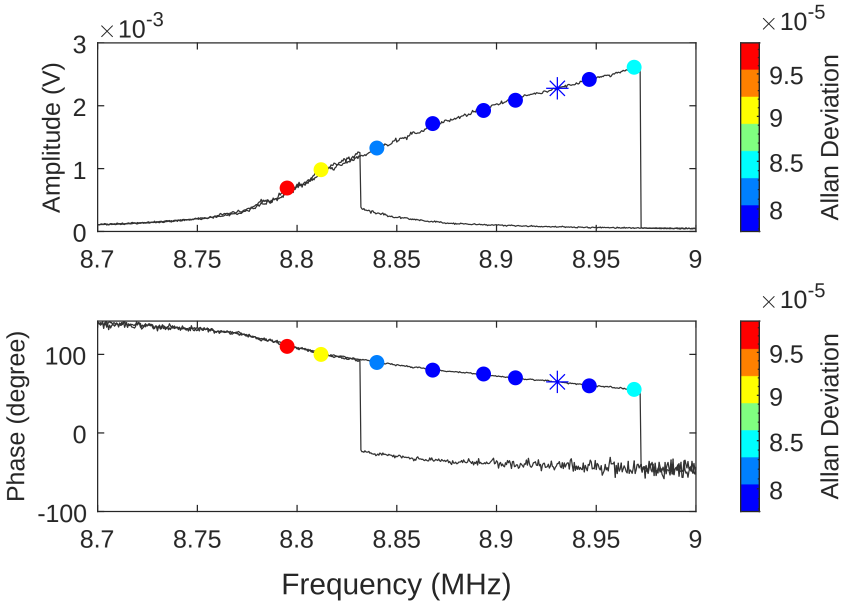

Figure A.15: Allan Deviation at the frequency response for drum 10_2.13.2

A.3.2. Drum 10_2.14.2

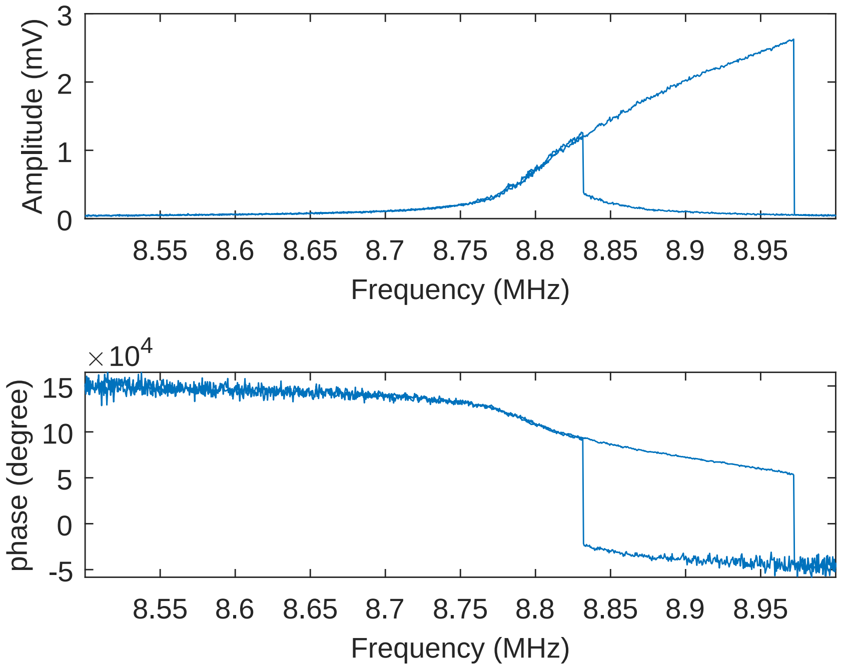

Figure A.16: Allan Deviation for drum 10_2.14.2 with a power of 5 dBm

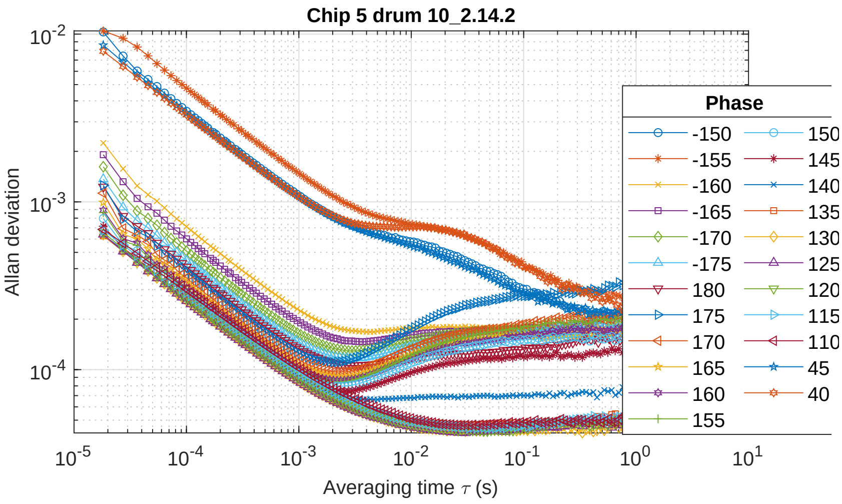

Figure A.17: Allan Deviation for drum 10_2.14.2

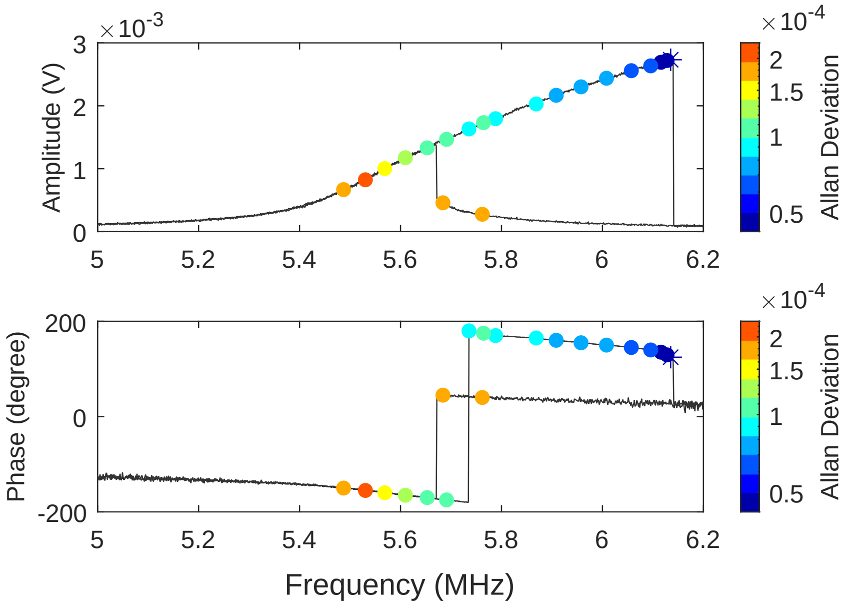

Figure A.18: Allan Deviation at the frequency response for drum 10_2.14.2

Frequency spectrum while PLL controlled

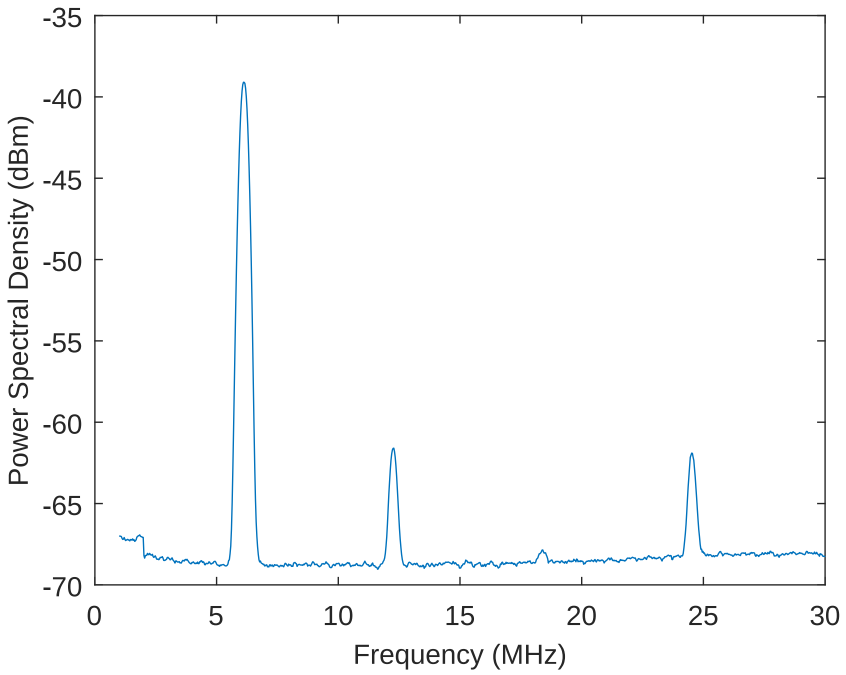

Figure A.19: Frequency Spectrum of drum 10_2.14.2 when controlling it at 105°

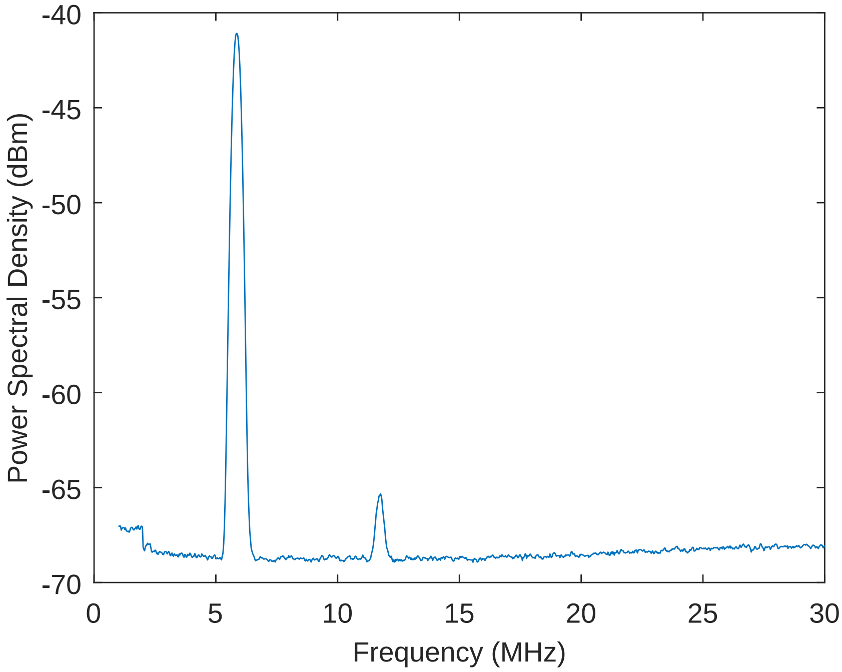

Figure A.20: Frequency Spectrum of drum 10_2.14.2 when controlling it at 150°

A.3.3. Drum 10_2.16.2

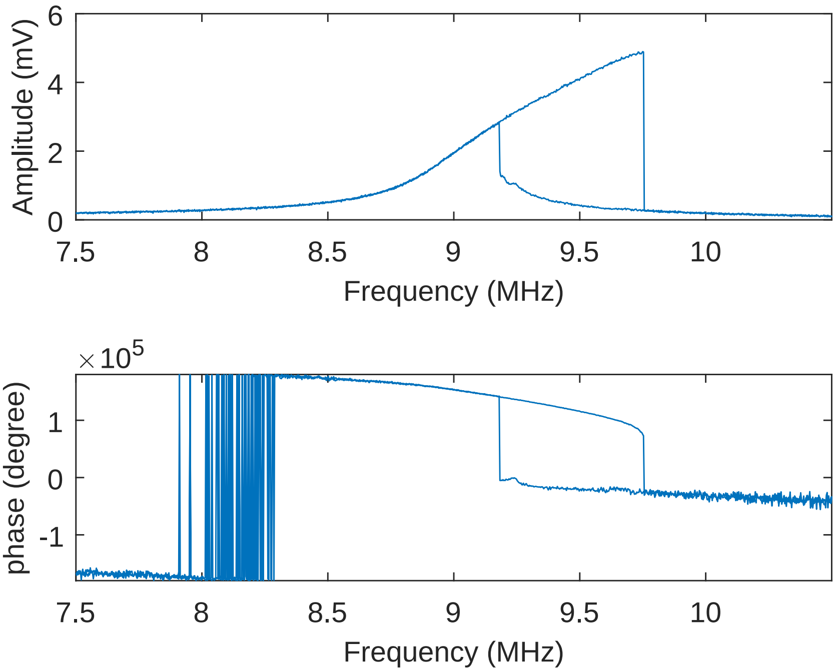

Figure A.21: Allan Deviation for drum 10_2.16.2 with a power of 5 dBm

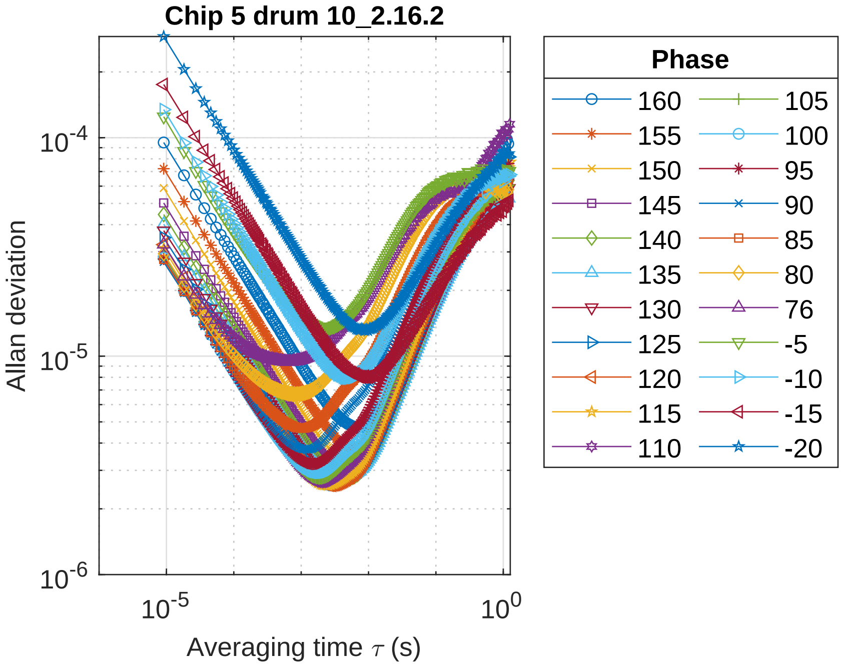

Figure A.22: Allan Deviation for drum 10_2.16.2

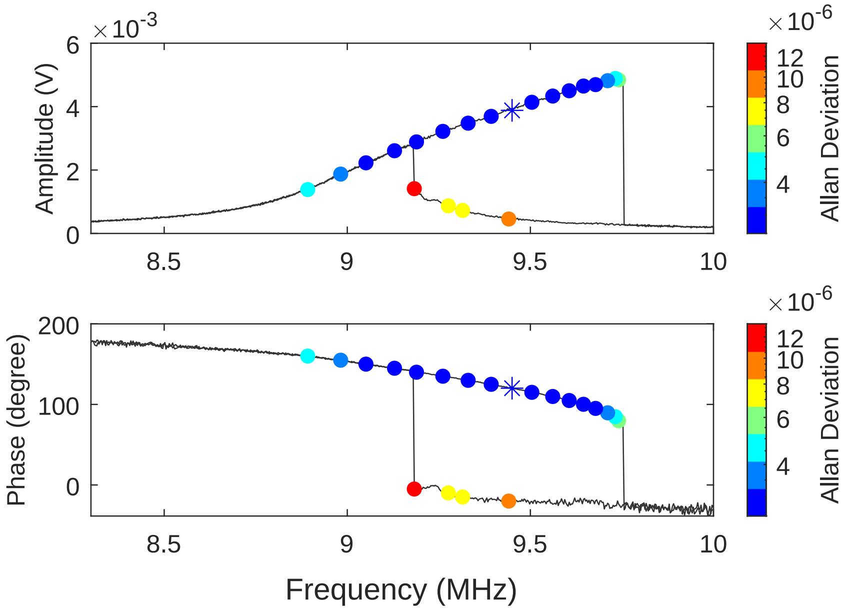

Figure A.23: Allan Deviation at the frequency response for drum 10_2.16.2

Backbone curve

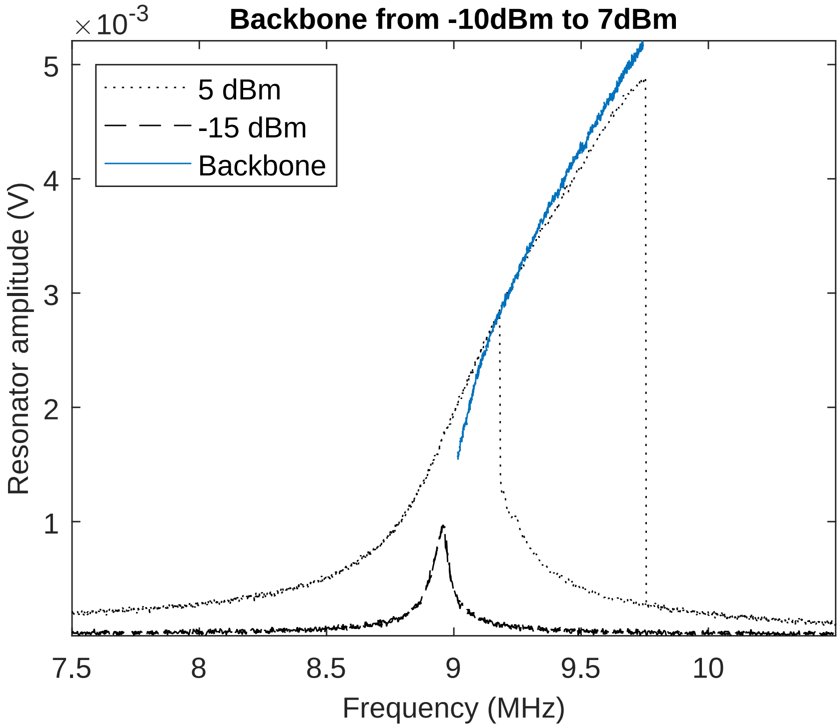

Figure A.24: Backbone curve acquired by sweeping the power from −10 dBm to 7 dBm while operating with PLL at setpoint of 76° for drum 10_2.16.2

B

Experimental procedures

This appendix contains additional information concerning the procedures used by the conducted experiments.

B.1. Graphene drum fabrication

This section explains the steps required to fabricate a graphene drum on a silicon chip with SiO_2 substrate. The fabrication of the silicon chip is not explained in this work.

B.1.1. Chip layout

The drum is stamped on a silicon chip with different hole sizes. Each row of grouped holes in fig. B.1 has holes with the same diameter: 10 µm, 8 µm, 6 µm, 4 µm and 2 µm, from top to bottom. The columns consist of different spacial distributions, so a flake of graphene can be positioned on one or multiple cavities. These cavities are etched in a layer of SiO_2 and have a depth of 285 nm.

Before a graphene flake can be stamped onto the chip, it needs to be synthesized.

B.1.2. From graphite to graphene

To achieve thin layers of graphite, a procedure generally known as the ”Scotch Tape method” [22] is used. For more details on this dry viscoelastic stamping method the reader is referred to [23]. By using adhesive tape, a thin layer of graphite is peeled off a piece of natural graphite. Subsequently, the material on the tape is further exfoliated using more adhesive tape to peel off the graphite layer by layer. This continues until the graphite flakes (i.e. the layers) are thin enough. This means usually that they are barely visible with the naked eye. In this work multilayer graphene is used to create drums. This means that the membranes are not exactly one atom thick, but contains multiple layers.

The next step is to transfer the freshly created flakes to the chip.

B.1.3. Transfer graphene to PDMS

In order to select and position a graphene flake onto the chip, it first needs to be transferred to a microscopic glass. Therefore, something is needed to attach the flake to the glass. A 0.5 cm square slice of Polydimethylsiloxane (PDMS) is placed onto one end of the microscopic glass to serve for this purpose. The flakes are transferred from the adhesive tape to the PDMS by pressing the glass with PDMS to the flakes on the tape, and then separate them again (make sure the PDMS stays on the glass!). This can be done multiple times to transfer more flakes.

Now is a good time to place the chip on the graphene transfer setup positioner, see (1) in fig. B.2. Turn on the vacuum pump to fix the chip to the stage.

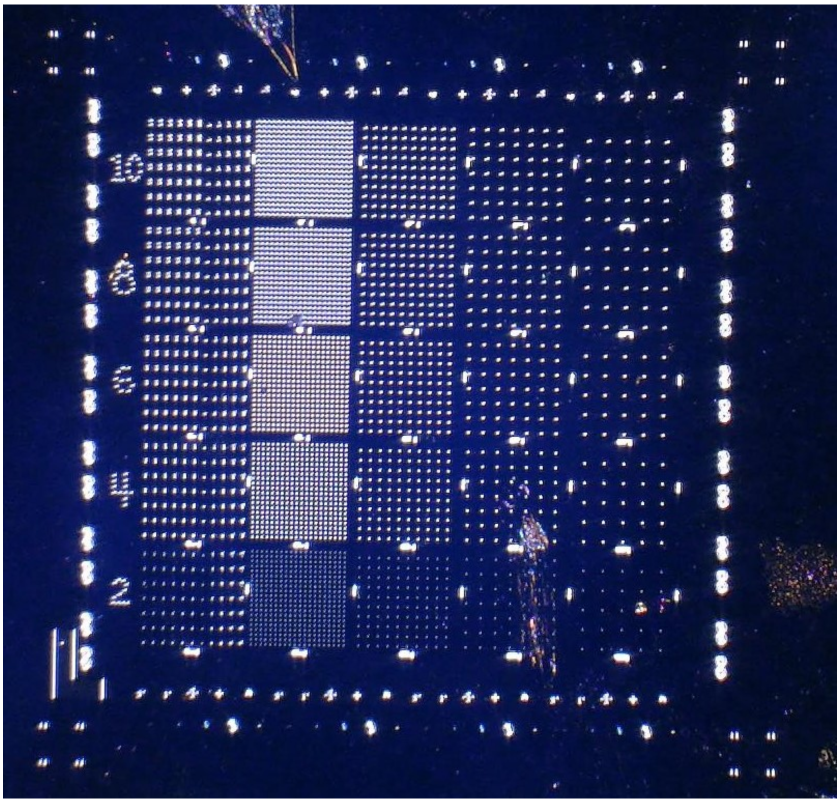

Figure B.1: Optical image of the chip. The numbers at the left are the size of the holes in the corresponding row. A bit of residual graphene is visible. Image by Irek Rosłoń.

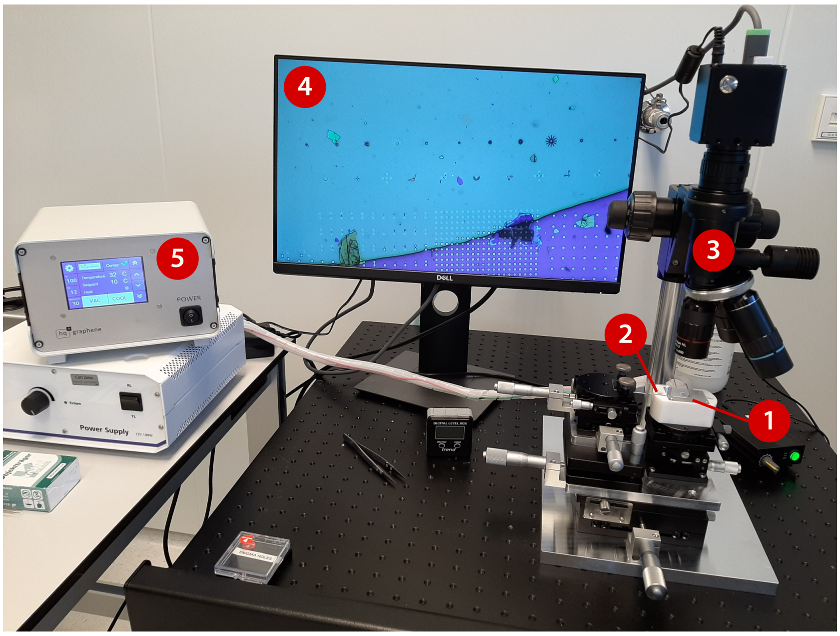

Figure B.2: 2D Heterostructure Transfer System from hq graphene. The chip is put on the stage (1) which can move independently of the microscopic glass with the PDMS and graphene flakes (2). The microscope (3) is used to visually inspect the position the flakes and the chip on the screen (4). The chip can be fixed to the stage by a vacuum pump and can be heated/cooled from the controller (5).

B.1.4. Select graphene flake

Next, the best flakes need to be selected. This can be done by using the microscope in the graphene transfer setup. Clamp the microscopic glass onto the positioner with the PDMS facing downwards. By scanning the PDMS for flakes, the best ones can be selected. In most cases the best ones have a greyish colour, as they don't reflect that much light from the microscope. Besides, they show no sign of ripples like lines crossing the flake itself.

B.1.5. Transfer the flake to the chip

Once a flake is selected, the chip is aligned so it covers the desired holes. Now the chip is slowly brought closer to the glass with PDMS. It is important to check if the relative position of the flake to the chip is still the desired one.

When the PDMS attaches to the chip, the colour of the chip changes for this region. It is important to look for this region, as it is vital that the selected flake is *slowly* attached to the chip. This region is brought close to selected flake by slowly moving the chip toward the microscopic glass.

At this point, expansion of the PDMS due to an increase in temperature can be used to slowly attach the flake to the chip. Increase the temperature setpoint slowly, only a couple of degrees Celsius at the time. It can take 5 min to 10 min (depending on the size of the flake) to extend the attachment region to fully cover the flake. Typically, one doesn't need to set the temperature setpoint higher than 45 °C.

The tricky part is separating the PDMS and the chip, while the flake stays attached to the chip. Therefore, it is important that it is done *slowly*, for example by cooling the chip down. This usually takes longer than heating it. When the flake is not in the attachment region anymore, the chip can be moved away from the PDMS.

This process can be repeated for other flakes. Be aware that stamping another flake to the chip can cause a flake that is already there to ripple or detach.

B.1.6. Make the chip ready for experiments

When there are sufficient drums stamped onto the chip, it can be used for experiments. Note that the chip is fixed by a vacuum, so turn off the vacuum pump and slide the chip over the stage with soft tweezers before picking it up. This way it one can be sure that the chip won't stick to the stage any more.

Table B.1: PLL parameters for tuning fork measurements

Field	Value	Unit
Filter BW	3.277	kHz
Filter order	4	-
Center	32.764	kHz
Upper and lower limit	±5	Hz
P	−5.718	$\text{Hz}\,°^{-1}$
I	−78.7	$\text{mHz}\,°^{-1}\,\text{s}^{-1}$
D	0	$\text{Hz}\,\text{s}\,°^{-1}$
Rate	3.516	MHz

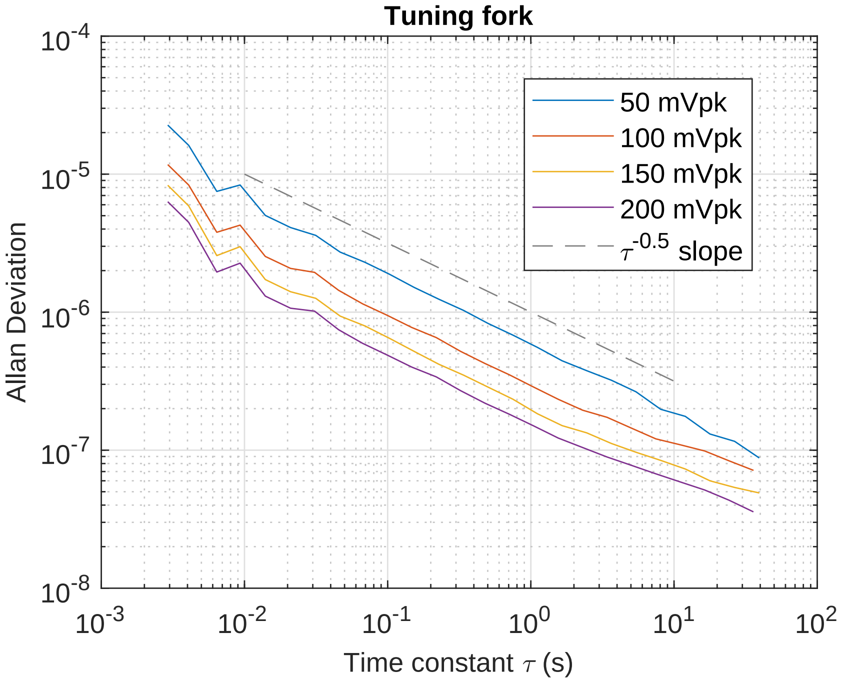

Figure B.3: Allan deviation for a tuning fork. The line labelled $\tau^{-0.5}$ represents the slope of the white phase noise in the Allan Deviation.

B.2. Validation of measurement and calculation of Allan Deviation

To make sure the whole procedure of tuning, recording and processing data from the setup is done in a correct way, the same measurements with a linear tuning fork were done. Because the properties of a tuning fork are known, it is possible to validate the measurement procedure. The tuning fork used is RS PRO 32.768kHz Crystal [1]. This tuning fork has a frequency tolerance of ±20 ppm.

B.2.1. Experiment

The tuning fork is wired up to the Zurich Instruments UHFLI and a frequency sweep is performed. Using the linear fitting functionality of the UHFLI the Q factor ($Q = 119 \times 10^3$), resonance frequency ($f_0 = 32.76$ kHz) and phase ($\phi_0 = 247.17 \times 10^{-3}°$) are determined. For the demodulator filter bandwidth and the PLL bandwidth a 10th and a 100th of the resonance frequency are used respectively. These values are then used to calculate the value of P and I according to appendix B.3.

The values are inserted to their corresponding fields within the PLL tab of the UHFLI. The demodulator filter order is set to 4, the frequency limit is set to ±5 Hz and the rate is set sufficiently high. The exact values can be found in table B.1.

---

[1] `https://nl.rs-online.com/web/p/crystal-units/1442305/`

Table B.2: Average resonance frequency of the tuning fork.

Excitation power	Mean frequency
50 mVpk	32 764.279 144 129 9 Hz
100 mVpk	32 764.270 017 001 7 Hz
150 mVpk	32 764.249 131 754 1 Hz
200 mVpk	32 764.237 607 797 0 Hz

For different forcing amplitudes (V_{pk}) of 50 mV, 100 mV, 150 mV and 200 mV, the PLL is active and the demodulation frequency is recorded for one hour with a sampling rate of 1.717 kHz. Next, the recorded data is supplied to the `allandev` function in MATLAB (see appendix E.1), resulting in fig. B.3.

B.2.2. Validation

From fig. B.3 it is shown that the frequency stability is limited by white phase noise (slope of $\tau^{-0.5}$), which is expected. This white phase noise indicates the frequency instability due to thermomechanical noise. As the data points for the lowest values of τ are influenced by the PLL bandwidth, the overall results have the expected slope. The reduction of the Allan Deviation for an increase in force is as predicted. An increase in force results in better signal-to-noise ratio which improves the frequency stability.

By inspecting the average demodulation frequency (which is the resonance frequency) for each measurement, one can see if the frequency tolerance from the specs is met. The 20 ppm frequency tolerance translates in a resonance frequency between 32 767.344 64 Hz and 32 768.655 36 Hz. However, the conducted measurements have a mean frequency outside this domain, see table B.2. From the measurement it is shown that the resonance frequency is at 32 764 Hz. Using this as the average frequency, the range of the averaged measured resonance frequency should be between 32 763.344 72 Hz and 32 764.655 28 Hz. The values in table B.2 are clearly within this domain and therefore meets the frequency stability from the specs.

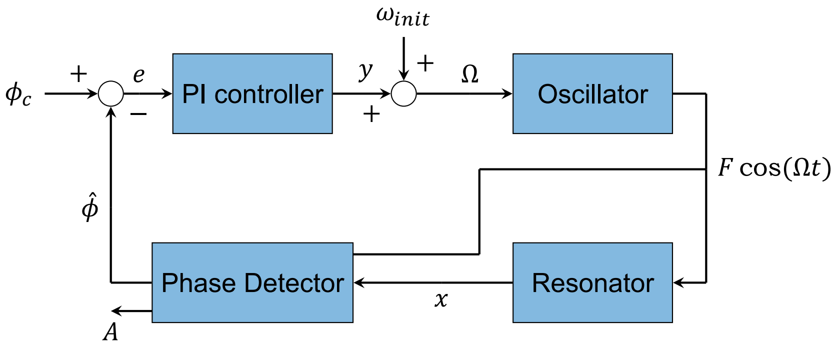

Figure B.4: Schematic representation of a resonator incorporated with a PLL. The oscillator generates a periodic signal with frequency Ω and amplitude F to drive the resonator. In the phase detector the response of the resonator is compared with the driving signal resulting in the estimated phase difference $\hat{\phi}$. This phase is then compared to the phase set-point ϕ_c and on this difference, the error, acts a PI controller. The resulting correction y of the controller is added to the initial driving frequency ω_{init} and proceeds as the oscillator frequency Ω.

B.3. PLL parameters selection

A phase locked loop (PLL) needs to be tuned in order to operate correctly. Tuning involves finding values for the PI controller, k_p and k_i, and determining the demodulator low pass filter bandwidth and order.

Values for the PI parameters are found by using the method by Denis *et al.* [9] or Olcum *et al.*. In the next sections the methods are explained and is demonstrated that the first method is not valid for graphene drums.
To determine the demodulator filter cut-off frequency f_c and the PLL bandwidth f_{pll}, a rule of thumb is used. This rule states $f_0 >> f_c >> f_{pll}$, which essentially means that a factor of 7 to 10 is between these frequencies. In this work, the factor 10 is used.

B.3.1. PI parameters by averaged equations

Denis *et al.* [9] use the method of averaging to find values for k_i that stabilize the system. Following along with both [9, 24], it starts with a set of differential equations, including a mathematical description of the PLL.

$$\ddot{x} + 2\zeta\omega_0\dot{x} + \omega_0^2 x + \gamma x^3 = F\cos(\theta) \tag{B.1a}$$

$$\dot{\theta} = \Omega = \omega_{init} + y \tag{B.1b}$$

$$\dot{y} = k_i(\hat{\phi} - \phi_c) \tag{B.1c}$$

$$\dot{\hat{\phi}} = \omega_c(\phi - \hat{\phi}) \tag{B.1d}$$

Besides the symbols used in main text and fig. B.4, ϕ is the actual phase shift between the forcing signal and the output signal and $\omega_c = f_c/2\pi$ is the cut-off frequency of the low pass filter incorporated in the phase detector. After averaging the Duffing equation in eq. (B.1) and solving for the fixed points, the equations are written in the jacobian matrix J. From here stability can be easily investigated by calculating the eigenvalues. The system is stable if the real parts of J are negative. This results in conditions for the value of k_i.

As the method of averaging is a perturbation method, it assumes that the nonlinearities as forces are small compared to the other parameters. From experiments it became clear that this is not the case for graphene drums. No values that where stable according tot the method where able to control a drum.

B.3.2. PI parameters using a linear model

For linear devices it is possible to find a transfer function for the resonator including the PLL. This has been done by Olcum *et al.* [25] and improved upon by Demir & Hanay [26]. To make it simple to control the bandwidth of the PLL (ω_{pll}), they set $k_p = \omega_{pll}$. To cancel this pole by an other zero, $k_i = k_p/\tau_c$ is

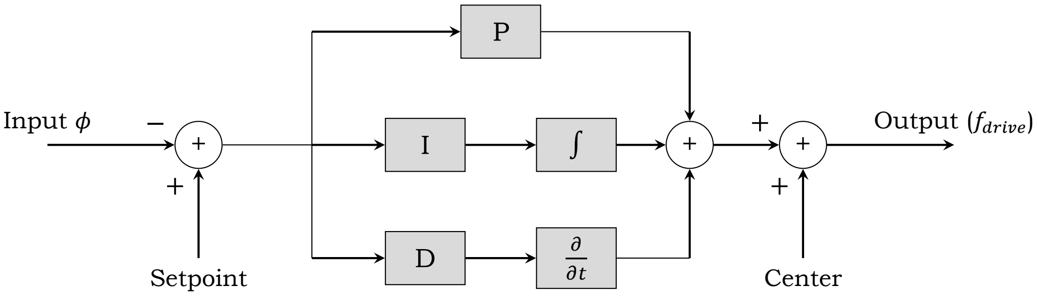

Figure B.5: PID block diagram. Simplified version from the manual [27]. The units of ϕ and the setpoint are degree and of the center and f_{drive} are in hertz. The PID parameters are constant gain blocks, marked with their corresponding letter.

used. Here is $\tau_c = 2Q/\omega_0$ the characteristic time of the resonator. This method can be a nice starting point to work at at least at the stable branch of the Duffing resonator.

Parameter unit conversion

To use these parameters in the UHFLI, they need to be converted, as the units are different in the device and from the paper by Olcum *et al.*. Appendix B.3.2 displays a simplified version of the UHFLI PID block diagram. In this image the input and setpoint have the unit degree and the center and output the unit hertz. Therefore the P, I and D parameters have units Hz $°^{-1}$, Hz $°^{-1}$ s^{-1} and Hz s $°^{-1}$ respectively. The units of the parameters of Olcum *et al.* have units rad s^{-1} and rad s^{-2} for k_p and k_i respectively. The unit conversion between these units and the UHFLI units (denoted by the superscript UHFLI) is shown in eq. (B.2). Note that also a minus sign is introduced for k_p^{UHFLI}. This because without it does not work.

$$\begin{aligned} k_p &= \omega_{pll}, \qquad & k_p^{UHFLI} &= -\frac{\omega_{pll}}{360}k_p = -\frac{2\pi}{360}f_{pll} \\ k_i &= \frac{k_p}{\tau_c} = k_p\frac{\omega_0}{2Q}, \qquad & k_i^{UHFLI} &= k_p^{UFHLI}\frac{\omega_0}{2Q} = k_p^{UHFLI}\frac{2\pi}{2Q}f_0 \end{aligned} \tag{B.2}$$

C

Simulations

The simulations are performed with a MATLAB Simulink model. This appendix shows the model and some results.

C.1. Simulink model

The model consists of a nonlinear Duffing equation incorporated in a PLL. An overview of the model is presented in fig. C.1. There are two subsystems, one representing the resonator and another one representing the phase detector. Some blocks require parameters. The important ones are `omega_init`, the initial excitation frequency in rad s^{-1}, `phase` the phase setpoint in rad, the PI parameters and the noise powers of the two band-limited white noise blocks. The one at the left represents the thermomechanical noise and the one at the bottom the amplitude noise. They are set to the values described in the main text.

C.1.1. Nonlinear resonator subsystem

This subsystem consists of two integrators which feed their results to a MATLAB function, see fig. C.2. This function calculates the second derivative which goes to the integrators again. The code in this MATLAB function is the following:

```matlab
function ddy  = fcn(u, y, dy, c, eta, k, gamma)
    ddy = u - c*dy - eta*dy*y^2 - k*y - gamma*y^3;
```

The parameters used are `c`, `eta`, `k` and `gamma`, which represent the linear damping, nonlinear damping, stiffness and cubic stiffness respectively.

C.1.2. Phase detector subsystem

The phase detector is modelled after [28] and its working principle is synchronous demodulation, see fig. C.3. In essence, the resonator response signal is multiplied with a sine and cosine signal at the same frequency as the excitation signal. This product is then led through a low-low-pass filter resulting in the in-phase (`Y`) and quadrature component (`X`). This low-pass filter is build from a zero-pole-gain model with the desired cut-off frequency and filter order that is converted to state space. The calculations of the state space values and initial conditions using the parameters `wh` (cut-off frequency) and `order` is presented below.

```matlab
%% Build Low Pass filter
z = []; % no zeros
p = ones(1, order) * (-wh); % all poles at -wh
g = wh^order; % a gain that makes the passband gain 1
lpf_tf = zpk(z,p,g);
lpf = canon(lpf_tf,'modal');
```

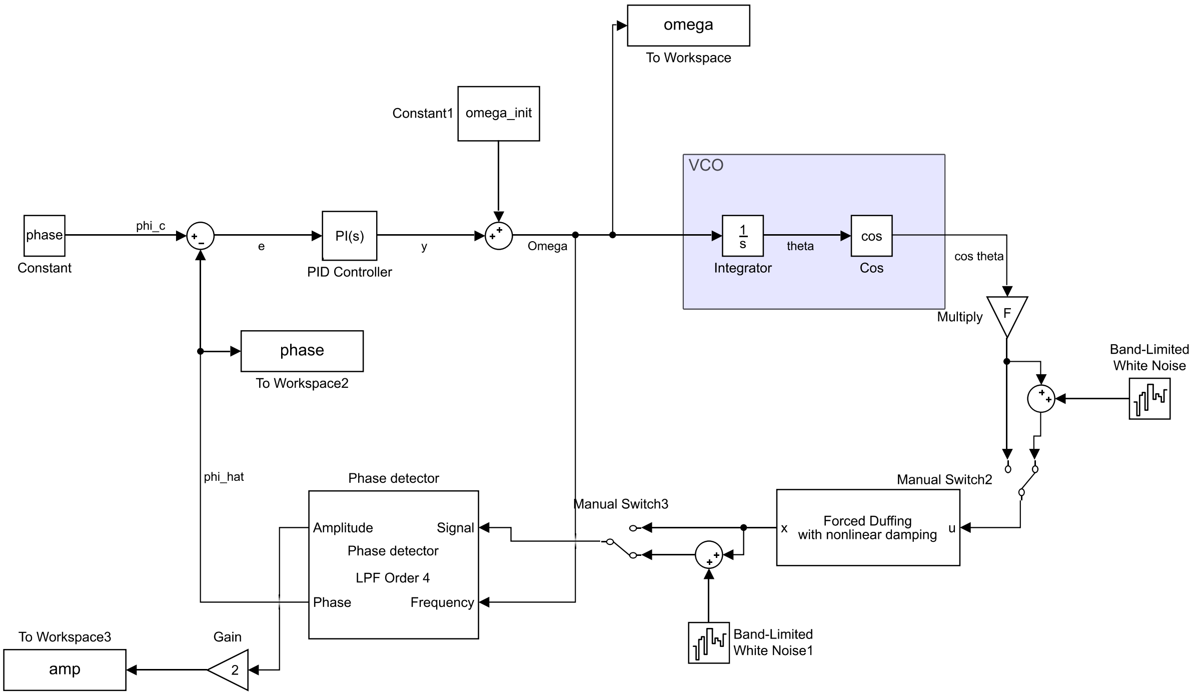

Figure C.1: Overview of the Simulink Simulation model

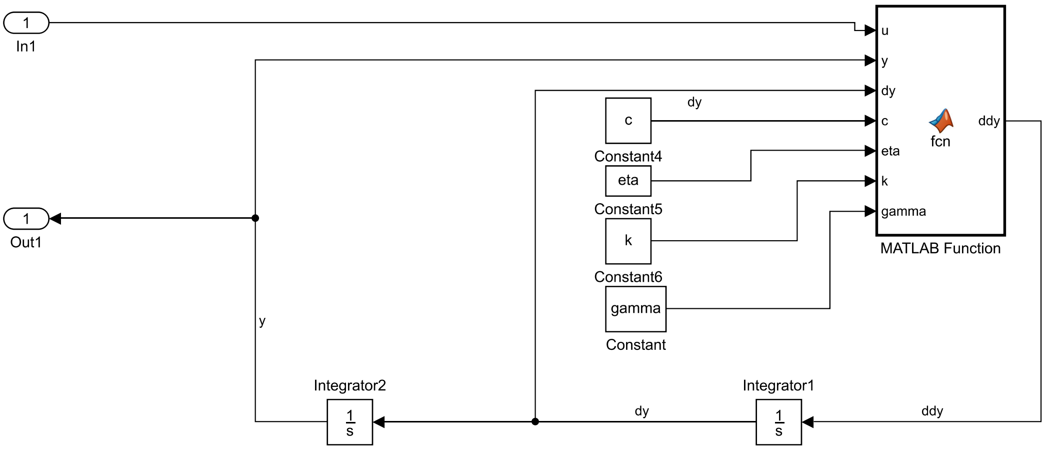

Figure C.2: The subsystem representing the nonlinear resonator.

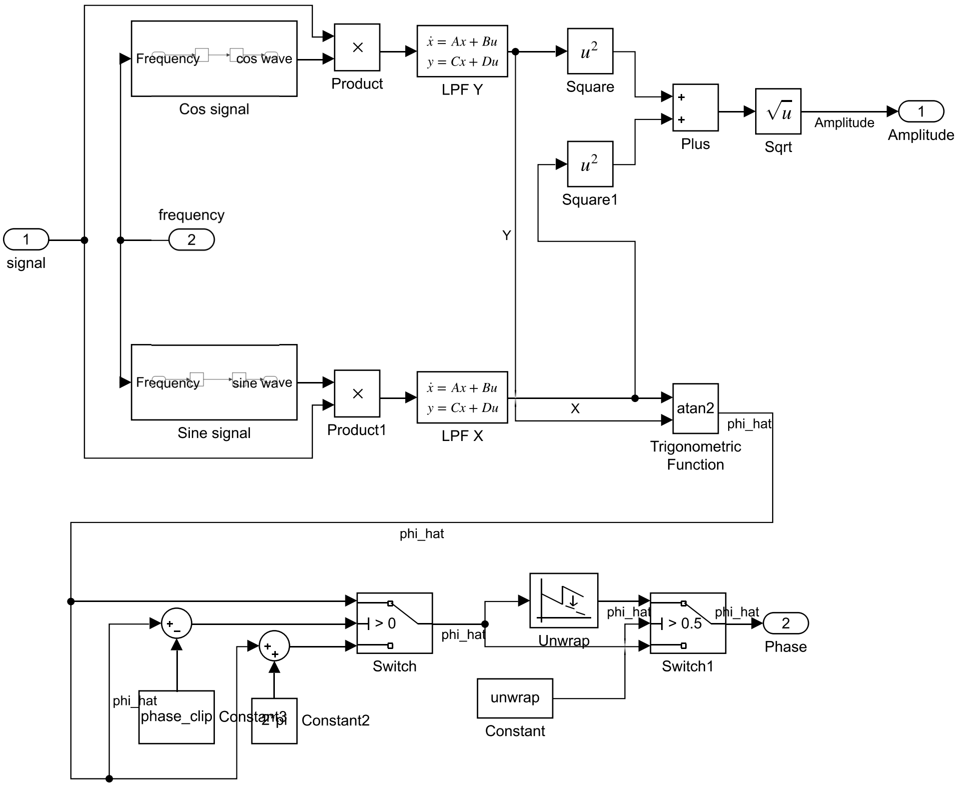

Figure C.3: The subsystem operating as the phase detector. It is modelled after [28].

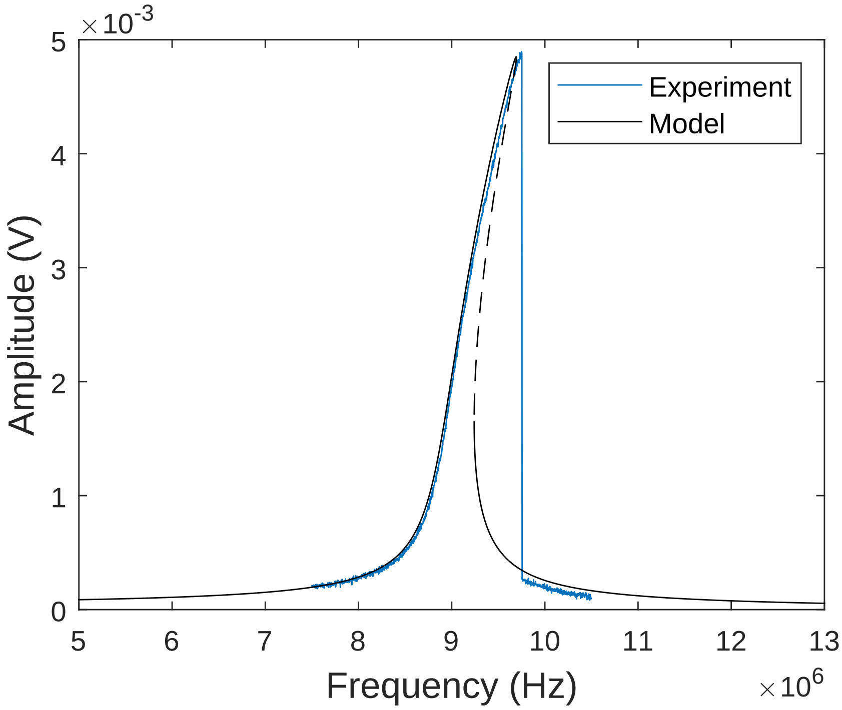

Figure C.4: The frequency response of the resonator model compared to one of an actual drum.

```
% initial conditions equeal to steady state
lpfY0 = -inv(lpf.A)*lpf.B;
% lpfY0 = zeros(1, order);
lpfX0 = zeros(1, order);
```

From these filtered signals the amplitude and phase are calculated. The additional blocks on the phase output are there to shift the phase clipping boundaries and to unwrap the phase if desired.

C.2. Simulation results

The results described in this section use the parameters mentioned in the main text.

C.2.1. Comparison of resonator model with experiment

To compare the resonator model with the experiments, AUTO97 [29] is used to generate the frequency response of the model. This is compared visually with a frequency response obtained from experiments, see fig. C.4.

C.2.2. Allan Deviation

In fig. C.5, the Allan Deviation is presented that results from the simulations. This simulation has run for 1×10^6 s simulation time, but this is 17.7 ms in normal time. This is also visible in the Allan Deviation as the lines are not smooth. Running the simulation longer will result in smoother Allan Deviation lines.

C.2.3. Nonlinear damping and force

What if the increased force when using a higher nonlinear damping value to compensate for the amplitude results in the better Allan Deviation? To check this all combinations of the two force levels and nonlinear damping values are plotted in fig. C.6. This figure shows that an increase in force improves the frequency stability. However, for higher phase values the frequency stability does not match the frequency stability of the increased nonlinear damping. Next to that, for phase setpoins higher than 40°, the frequency stability improves more than without increased nonlinear damping.

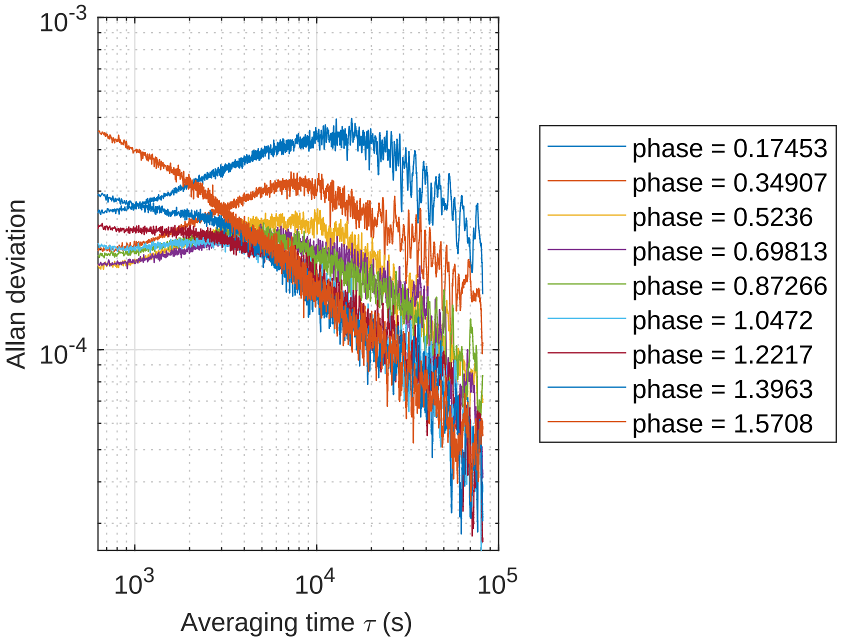

Figure C.5: Allan Deviation resulting from the simulations.

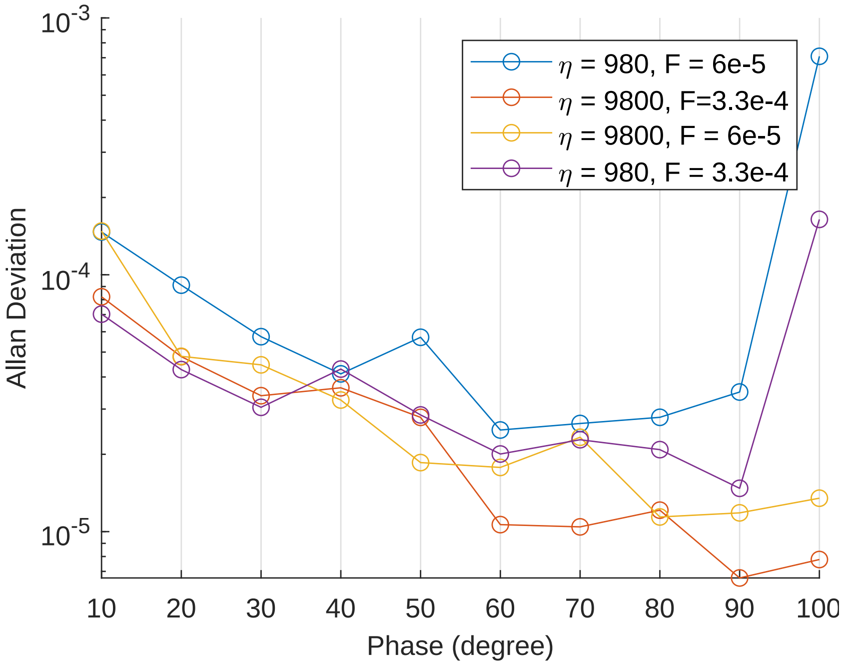

Figure C.6: Minimal Allan Deviation for each phase setpoint for different nonlinear damping values and excitation force levels.

D

Derivations of resonator frequency responses

This appendix contains the derivation of the linear and nonlinear frequency responses.

D.1. Frequency response of a forced harmonic resonator

The forced harmonic resonator can be used as a model for a linear resonator.

$$\ddot{x} + 2\zeta\omega_n\dot{x} + \omega_n^2 x = F\cos(\Omega t) \tag{D.1}$$

To find the amplitude and frequency response we find a solution for eq. (D.1), a non-homogenous linear differential equation, following along with [14, 30]. To find the amplitude and the phase in the steady state, only the particular solution is required as the homogenous solution decays away over time. Because the amplitude and phase are of interest, a solution is sought in the form of

$$x_p(t) = A\cos(\Omega t - \theta) \tag{D.2}$$

where A and θ represent the amplitude and the phase respectively. Ω is the same forcing frequency as used in eq. (D.1). This solution and its derivatives are substituted into eq. (D.1), resulting in eq. (D.3).

$$-\Omega^2 A\cos(\Omega t - \theta) - 2\zeta\omega_n\Omega A\sin(\Omega t - \theta) + \omega_n^2 A\cos(\Omega t - \theta) = F\cos(\Omega t) \tag{D.3}$$

$$\sin(\Omega t - \theta) = \sin(\Omega t)\cos(\theta) - \cos(\Omega t)\sin(\theta) \tag{D.4a}$$

$$\cos(\Omega t - \theta) = \cos(\Omega t)\cos(\theta) + \sin(\Omega t)\sin(\theta) \tag{D.4b}$$

To collect all the $\sin$ and $\cos$ terms, the trigonometric function in the particular solution can be rewritten as the in-phase and quadrature components, see eq. (D.4). Doing so, i.e. substituting the equations from eq. (D.4) into eq. (D.3), yields the following result.

$$\begin{aligned}\cos(\Omega t)\big[-\Omega^2 A\cos(\theta) - 2\zeta\omega_n\Omega A\sin(\theta) + \omega_n^2 A\cos(\theta) - F\big]\\ + \sin(\Omega t)\big[-\Omega^2 A\sin(\theta) - 2\zeta\omega_n\Omega A\cos(\theta) + \omega_n^2 A\sin(\theta)\big] = 0\end{aligned} \tag{D.5}$$

As it is expected that the condition in eq. (D.5) holds for all values of t, each of the two parts between the square brackets have to be equal to zero. The two resulting equations will lead to an expression for the amplitude and the phase of the resonator.

$$-\Omega^2 A\cos(\theta) - 2\zeta\omega_n\Omega A\sin(\theta) + \omega_n^2 A\cos(\theta) - F = 0 \tag{D.6a}$$

$$-\Omega^2 A\sin(\theta) - 2\zeta\omega_n\Omega A\cos(\theta) + \omega_n^2 A\sin(\theta) = 0 \tag{D.6b}$$

Starting with eq. (D.6a), one can get rid of the $\sin(\theta)$ and $\cos(\theta)$ by visualizing the expression as a vector with length F and angle θ. The adjacent and the opposite sides of the triangle that this vector describes have a length of the expression before $\sin(\theta)$ and $\cos(\theta)$.Therefore, the lengths are $(\omega_n^2 - \Omega^2)A$ and $-2\zeta\omega_n\Omega A$ of the adjacent and opposite side respectively. Now the lengths of all the sides of the triangle are known, the Pythagorean theorem can be applied.

$$((\omega_n^2 - \Omega^2)A)^2 + (-2\zeta\omega_n\Omega A)^2 = F^2 \tag{D.7}$$

Rearranging eq. (D.7) and solving it for A results in an expression for the amplitude for a given driving frequency Ω.

$$A(\Omega) = \frac{F}{\sqrt{(\omega_n^2 - \Omega^2)^2 + (-2\zeta\omega_n\Omega)^2}} \tag{D.8}$$

To find an expression for the phase, eq. (D.6b) is used. After grouping the coefficients by $\sin(\theta)$ and $\cos(\theta)$, the expression in eq. (D.9) can be written.

$$\frac{\sin(\theta)}{\cos(\theta)} = \frac{2\zeta\omega_n\Omega A}{(\omega_n^2 - \Omega^2)A} = \tan(\theta) \tag{D.9}$$

By cancelling out the A and taking the inverse tangent, the expression for the phase as a function of the driving frequency is found.

$$\theta(\Omega) = \arctan\left(\frac{2\zeta\omega_n\Omega}{\omega_n^2 - \Omega^2}\right) \tag{D.10}$$

D.2. Frequency response of a forced Duffing resonator

To model nonlinear primary resonance, a forced Duffing resonator can be used as a model.

$$\ddot{x} + 2\zeta\dot{x} + x + \gamma x^3 = F\cos(\Omega t) \tag{D.11}$$

To find the forced frequency response of the resonator presented in eq. (D.11), the Krylov–Bogolyubov method of averaging is used, following [31–35]. This is a perturbation method which means it assumes a weakly nonlinear system. This means that the following derivation is valid for small values of ζ, γ and F.

$$\ddot{x} + x\epsilon\bar{h}(x,\dot{x},t) = 0 \tag{D.12}$$

One starts with an equation in that looks like eq. (D.12). Here is $0 < \epsilon << 1$ the small parameter that suffices the assumption of a weakly nonlinear system. To match eq. (D.12) with eq. (D.11), an expression for $\bar{h}(x,\dot{x},t)$ needs to be established.

$$\bar{h}(x,\dot{x},t) = 2\bar{\zeta}\dot{x} + \bar{\gamma}x^3 - \bar{F}\cos(\Omega t) \tag{D.13}$$

The parameters with a bar above it represent the values of these parameters of $\mathcal{O}(1)$, while without bar the values are of $\mathcal{O}(\epsilon)$. They are related as $\zeta = \epsilon\bar{\zeta}$, $\gamma = \epsilon\bar{\gamma}$ and $F = \epsilon\bar{F}$. Substituting eq. (D.13) into eq. (D.12) results in the equation of concern, eq. (D.11).

Now eq. (D.12) is converted to state space in eq. (D.14). Now a solution is presented for $\epsilon = 0$, as it were the linear case, see eq. (D.15).

$$\begin{cases} \dot{x} = y \\ \ddot{x} = \dot{y} = -x - \epsilon\bar{h}(x,y,t) \end{cases} \tag{D.14}$$

$$x = A\cos(t+\theta) \quad , \quad y = -A\sin(t+\theta) \tag{D.15}$$

The symbols A and θ are the amplitude and phase of oscillation respectively. They are defined as the polar representation of x and y, see eq. (D.16).

$$x^2 + y^2 = A^2 \tag{D.16a}$$

$$\theta + t = -\arctan(\frac{y}{x}) \tag{D.16b}$$

In the linear case, A and θ are constant. But for a nonlinear resonator they change slowly (compared to the oscillations) over time. So for $\epsilon > 0$, $A \rightarrow A(t)$ and $\theta \rightarrow \theta(t)$ is assumed. The goal is to find approximations for the change of these parameters over time. Therefore, by definition eq. (D.14) stays the same although A and θ are now considered to be time dependent.

By taking the derivative with respect to time of eq. (D.16a) and eq. (D.16a) and then substituting eq. (D.14) and eq. (D.15) to come up with an expression without x and y, see eq. (D.17).

$$\dot{A} = \epsilon \bar{h} \sin(t+\theta) \tag{D.17a}$$
$$A\dot{\theta} = \epsilon \bar{h} \cos(t+\theta) \tag{D.17b}$$

The following step is to substitute eq. (D.13) into eq. (D.17) and makes sure all references to x and y are substituted. Starting with eq. (D.17a) to do this and defining $\beta = t + \theta$, $\Omega = 1 + \epsilon\sigma$ and $\alpha = \theta - \epsilon\sigma t$, results in eq. (D.18). Here is σ a small parameter (therefore multiplied with ϵ) that can be varied around the resonance frequency, which is 1 in this case.

$$\dot{A} = \epsilon\left(-2\bar{\zeta}A\sin^2(\beta) + \bar{\gamma}A^3\cos^3(\beta)\sin(\beta) - \bar{F}\cos(\beta)\cos(\alpha)\sin(\beta) - \bar{F}\sin^2(\beta)\sin(\alpha)\right) \tag{D.18}$$

F appears twice in eq. (D.18) because of the expansion $\cos(\beta - \alpha) = \cos(\beta)\cos(\alpha) + \sin(\beta)\sin(\alpha)$.

This is where the averaging comes in. To remove the fast dynamics from the equation, they are averaged. The averaged value of a function is denoted by a bar or <> and defined as in eq. (D.19).

$$\bar{f} =< f(t) >= \frac{1}{2\pi}\int_{t-\pi}^{t+\pi} f(s)ds \tag{D.19}$$

When applying this to eq. (D.18) and noting $< \sin^2(\beta) >= \frac{1}{2}$ and $< \sin(\beta)\cos(\beta) >= 0$, it results in eq. (D.20).

$$\begin{aligned}\dot{\bar{A}} &= \epsilon\Big(-2\bar{\zeta}A < \sin^2(\beta) > +\bar{\gamma}A^3 < \cos^3(\beta)\sin(\beta) > \\ &\qquad -\bar{F} < \cos(\beta)\sin(\beta) > \cos(\alpha) - \bar{F} < \sin^2(\beta) > \sin(\alpha)\Big) \\ &= \epsilon\left(-\bar{\zeta}A - \frac{1}{2}\bar{F}\sin(\alpha)\right)\end{aligned} \tag{D.20}$$

As expected, $\dot{\bar{A}}$ is $\mathcal{O}(\epsilon)$, which is also the error compared to the exact solution.

The same procedure can be applied to eq. (D.17b), eventually resulting in eq. (D.21).

$$A\dot{\bar{\theta}} = \epsilon\left(\frac{3}{8}\bar{\gamma}A^3 + \frac{1}{2}\bar{F}\cos(\alpha)\right) \tag{D.21}$$

By remembering that $\theta = \alpha + \epsilon\sigma t$ and its time derivative $\dot{\theta} = \dot{\alpha} + \epsilon\sigma$, eq. (D.21) can be written as eq. (D.22).

$$A\dot{\alpha} = \epsilon\left(\frac{3}{8}\bar{\gamma}A^3 - \sigma A + \frac{1}{2}\bar{F}\cos(\alpha)\right) \tag{D.22}$$

At this point, the slow dynamics of the phase and amplitude are known. To construct a frequency response, the steady state is of interest and therefore the fixed points of these slow dynamics. These fixed points can be found by evaluating $\dot{\bar{A}} = 0$ and $\dot{\alpha} = 0$. Doing so and getting rid of ϵ by substituting the original parameters results in the following two equations.

$$\zeta A = -\frac{1}{2}F\sin(\alpha) \tag{D.23a}$$
$$\frac{3}{8}\gamma A^3 - \sigma A = -\frac{1}{2}F\cos(\alpha) \tag{D.23b}$$

To combine eq. (D.23a) and eq. (D.23b), they are squared and added up which results, after rearranging, in the forced frequency response function for the amplitude, see eq. (D.24).

$$\sigma = \frac{3}{8}\gamma A^2 \pm \sqrt{\frac{F^2}{4A^2} - \zeta^2} \tag{D.24}$$

An expression for the phase can be found similarly. The averaged phase is α, as the fast time oscillations are averaged out. By dividing eq. (D.23a) by eq. (D.23b), see eq. (D.25) results in the frequency response for the phase in eq. (D.26).

$$\frac{\zeta A}{\frac{3}{8}\gamma A^3 - \sigma A} = \frac{-\frac{1}{2}F\sin(\alpha)}{-\frac{1}{2}F\cos(\alpha)} = \tan\alpha \tag{D.25}$$

$$\alpha = \arctan\left(\frac{\zeta}{\frac{3}{8}\gamma A^2 - \sigma}\right) \tag{D.26}$$

Note: to match the phase direction of the linear resonator, eq. (D.26) needs to be multiplied with -1.

E

Code

This appendix contains a selection of the MATLAB code used in this thesis. All the MATLAB code is available at `https://doi.org/10.4121/13055690`.

E.1. Function `allandev`

```
function [sigma, tau, M] = allandev(freqSignal, sampleFreq, varargin)
%ALLANDEV Returns the allan deviation for the given frequency signal and
%sample frequency.
%
%       Author: Ties Verschuren (c) 2019
%
%[sigma, tau, M] = allandev(freqSignal, sampleFreq, ___)
%
%   INPUT
%       freqSignal      Frequency signal to calculate the allan deviation
%                       from.
%       sampleFreq      Sample frequency: used to calculate tau values.
%                       Expected unit: Hz
%   OPTIONAL INPUT (___)
%       minSamples      The minimal values to average over for sigma,
%                       default 100.
%       minGateTime     Minimal gate time to start from, default smallest
%                       possible (1/sampleFreq).
%       quiet           Disable progress output. Default true. When set to
%                       false, some progress data is shown.
%
%   OUTPUT
%       sigma           The allan deviation. (2 sample method)
%       tau             The gate times for which the allan deviation is
%                       calculated.
%       M               The number of samples used per gate time in the
%                       calculation.

%% Default values for optional parameters
minSamples = 100; %minimal 100
minGateTime = 1/sampleFreq;
pointsPerDecade = 5;
quiet = true;

%% parse optional parameters
if nargin > 2
    for i = 1:2:(nargin - 2)
        if size(varargin) < (i + 1)
            error('allandev: No value given for optional parameter %s', varargin{i});
        end
        value = varargin{i+1};
        switch varargin{i}
```

```
            case 'minSamples'
                minSamples = value;
            case 'minGateTime'
                minGateTime = value;
            case 'pointsPerDecade'
                pointsPerDecade = value;
            case 'quiet'
                quiet = value;
            otherwise
                error('allandev: Unknown option "%s" given.', varargin{i});
        end
    end
end

%% Parameter validation
if ~isnumeric(minSamples) || minSamples < 0
    error('allandev: Parameter minSamples should be a positive number, got %s', minSamples)
end

if ~isnumeric(minGateTime) || minGateTime < 0
    error('allandev: Parameter minGateTime should be a positive number, got %s', minSamples)
end

if ~isnumeric(pointsPerDecade) || pointsPerDecade < 0
    error('allandev: Parameter pointsPerDecade should be a positive number, got %s', pointsPerDecade)
end

if ~islogical(quiet)
    error('allandev: Parameter quiet should be a logical value (i.e. 1 or 0), got %s', quiet);
end


%% Calculate initial values
numSamples = numel(freqSignal);
freqAvg = mean(freqSignal); % average frequency

% Take the frequency fraction:  normalized frequency values to their mean.
y = freqSignal ./ freqAvg;

% Number of loops (number of different gate times used)
startTauNum = max(round(minGateTime * sampleFreq), 1); % starting index for gate time
endTauNum = max(floor(numSamples / (minSamples + 1 )), 1);

%% Calculate evaluation points
startTau = startTauNum * 1/sampleFreq;
endTau = endTauNum * 1/sampleFreq;
decades = log10(endTau) - log10(startTau);
evaluationTaus = logspace(log10(startTau), log10(endTau), round(decades * (pointsPerDecade + 1)));
evaluationPoints = unique(round(evaluationTaus * sampleFreq));
numPoints = numel(evaluationPoints);

%% Show status if needed
nbytes = 0;
if ~quiet
    fprintf('allandev: calculate for %d points\n', numPoints); % print status message
end

%% Initialize empty loop variables
sigma = zeros(numPoints, 1);
tau = sigma;
M = sigma;

%% Calculation
for i = 1:numPoints
    sampleIdx = evaluationPoints(i);
    % Tau is the time
    tau(i) = (1/sampleFreq) * sampleIdx;
    % num samples is always the number of average bins minus 1
    M(i) = floor(numSamples / sampleIdx) - 1;
    % sum for this tau value
    loopSum = 0;
```

```
    % Average for the first bin
    mm = 1;
    y_m = mean( y((1+(mm-1)*sampleIdx):(mm*sampleIdx)) );
    % loop over the other bins
    for m = 1:M(i)
        y_mplus1 = mean( y((1+m*sampleIdx):((m+1)*sampleIdx)) );
        loopSum = ((y_mplus1 - y_m)^2)/2 + loopSum;
        % store the average for the next loop
        y_m = y_mplus1;
    end
    % Calculate the allan deviation
    sigma(i) = sqrt( loopSum /(M(i)+1) );

    if ~quiet
        fprintf(repmat('\b',1,nbytes))
        nbytes = fprintf('allandev: pocessed %.2f %%\n', i/numPoints*100); % print status message
    end
end
% fprintf(repmat('\b',1,nbytes))
if ~quiet
    fprintf('allandev: Done\n');
end
end
```

Bibliography

[1] H. G. Craighead. Nanoelectromechanical systems. *Science*, 290(5496):1532–6, 2000. ISSN 0036-8075 (Print) 0036-8075 (Linking). doi: 10.1126/science.290.5496.1532. URL `https://www.ncbi.nlm.nih.gov/pubmed/11090343`.

[2] A. K. Geim and K. S. Novoselov. The rise of graphene. *Nat Mater*, 6(3):183–91, 2007. ISSN 1476-1122 (Print) 1476-1122 (Linking). doi: 10.1038/nmat1849.

[3] Anindya Nag, Arkadeep Mitra, and Subhas Chandra Mukhopadhyay. Graphene and its sensor-based applications: A review. *Sensors and Actuators A: Physical*, 270:177–194, 2018. ISSN 09244247. doi: 10.1016/j.sna.2017.12.028.

[4] Changyao Chen, Sami Rosenblatt, Kirill I. Bolotin, William Kalb, Philip Kim, Ioannis Kymissis, Horst L. Stormer, Tony F. Heinz, and James Hone. Performance of monolayer graphene nanomechanical resonators with electrical readout. *Nature Nanotechnology*, 4(12):861–867, 2009. ISSN 1748-3395. doi: 10.1038/nnano.2009.267.

[5] Zulfiqar H. Khan, Atieh R. Kermany, Andreas Öchsner, and Francesca Iacopi. Mechanical and electromechanical properties of graphene and their potential application in mems. *Journal of Physics D: Applied Physics*, 50(5), 2017. ISSN 0022-3727 1361-6463. doi: 10.1088/1361-6463/50/5/053003.

[6] A. Z. Hajjaj, N. Jaber, S. Ilyas, F. K. Alfosail, and M. I. Younis. Linear and nonlinear dynamics of micro and nano-resonators: Review of recent advances. *International Journal of Non-Linear Mechanics*, 119, 2020. ISSN 00207462. doi: 10.1016/j.ijnonlinmec.2019.103328.

[7] Ron Lifshitz and M. C. Cross. *Nonlinear Dynamics of Nanomechanical Resonators*, pages 221–266. Wiley, 2010. ISBN 9783527629374 9783527407910. doi: 10.1002/9783527629374.ch8.

[8] Rassul Karabalin. *Nonlinear and Parametric NEMS Resonators*, book section Chapter 101003-1, pages 1–13. Springer Netherlands, Dordrecht, 2015. ISBN 978-94-007-6178-0. doi: 10.1007/978-94-007-6178-0_101003-1.

[9] V. Denis, M. Jossic, C. Giraud-Audine, B. Chomette, A. Renault, and O. Thomas. Identification of nonlinear modes using phase-locked-loop experimental continuation and normal form. *Mechanical Systems and Signal Processing*, 106:430–452, 2018. ISSN 0888-3270. doi: 10.1016/j.ymssp.2018.01.014.

[10] Marc Sansa, Eric Sage, Elizabeth C. Bullard, Marc Gély, Thomas Alava, Eric Colinet, Akshay K. Naik, Luis Guillermo Villanueva, Laurent Duraffourg, Michael L. Roukes, Guillaume Jourdan, and Sébastien Hentz. Frequency fluctuations in silicon nanoresonators. *Nature Nanotechnology*, 11 (6):552–558, 2016. ISSN 1748-3387. doi: 10.1038/nnano.2016.19.

[11] S. Schmid, L. G. Villanueva, and M. L. Roukes. *Fundamentals of nanomechanical resonators*. Fundamentals of Nanomechanical Resonators. Springer International Publishing, 2016. ISBN 9783319286914 (ISBN); 9783319286891 (ISBN). doi: 10.1007/978-3-319-28691-4.

[12] Sidhant Tiwari and Rob N. Candler. Using flexural mems to study and exploit nonlinearities: a review. *Journal of Micromechanics and Microengineering*, 29(8):083002, 2019. ISSN 0960-1317. doi: 10.1088/1361-6439/ab23e2.

[13] R. van Leeuwen. *Nanoscale mechanical resonators and oscillators*. Ph.d. dissertation, Delft University of Technology, 2015.

[14] Mohammad I. Younis. *MEMS Linear and Nonlinear Statics and Dynamics*. Microsystems. Springer Science+Business Media, 2011. ISBN 978-1-4419-6019-1 978-1-4419-6020-7. doi: 10.1007/978-1-4419-6020-7.

[15] Ron Lifshitz and M. C. Cross. Nonlinear dynamics of nanomechanical and micromechanical resonators. In Heinz Georg Schuster, editor, *Reviews of Nonlinear Dynamics and Complexity*, pages 1–52. Wiley, 2008. doi: 10.1002/9783527626359.ch1.

[16] Oliver Brand, Isabelle Dufour, Stephen Heinrich, Fabien Josse, Gary K. Fedder, Christofer Hierold, Jan G. Korvink, and Osamu Tabata. *Resonant MEMS : Fundamentals, Implementation, and Application*. Wiley, Hoboken, 2015. ISBN 9783527676354.

[17] Ivana Kovacic and Michael J. Brennan. *The Duffing equation : Nonlinear Oscillators and their Behaviour*. Wiley, Oxford, 2011. ISBN 9780470715499. doi: 10.1002/9780470977859.

[18] Fritz. Riehle. *Frequency Standards: Basics and Applications*. Frequency Standards: Basics and Applications. Wiley Blackwell, 2003. ISBN 9783527605996. doi: 10.1002/3527605991.

[19] F. L. Walls and D. W. Allan. Measurements of frequency stability. *Proceedings of the IEEE*, 74(1): 162–168, 1986. ISSN 0018-9219. doi: 10.1109/proc.1986.13429.

[20] Věnceslav F. Kroupa. *Frequency stability : introduction and applications*. IEEE Press ; Wiley, Piscataway, NJ Hoboken, N.J., 2012. ISBN 9781118310144. doi: 10.1002/9781118310144.

[21] Karl J. Åström and Richard. M. Murray. *Feedback systems: An introduction for scientists and engineers*. Princeton University Press, New Jersey, 2008. ISBN 9780691135762. doi: 10.2307/j.ctvcm4gdk.

[22] Edward P. Randviir, Dale A. C. Brownson, and Craig E. Banks. A decade of graphene research: production, applications and outlook. *Materials Today*, 17(9):426–432, 2014. ISSN 13697021. doi: 10.1016/j.mattod.2014.06.001.

[23] Andres Castellanos-Gomez, Michele Buscema, Rianda Molenaar, Vibhor Singh, Laurens Janssen, Herre S. J. van der Zant, and Gary A. Steele. Deterministic transfer of two-dimensional materials by all-dry viscoelastic stamping. *2D Materials*, 1(1), 2014. ISSN 2053-1583. doi: 10.1088/2053-1583/1/1/011002.

[24] Mingxuan Fan, Matthew Clark, and Z. C. Feng. Implementation and stability study of phase-locked-loop nonlinear dynamic measurement systems. *Communications in Nonlinear Science and Numerical Simulation*, 12(7):1302–1315, 2007. ISSN 10075704. doi: 10.1016/j.cnsns.2006.01.018.

[25] S. Olcum, N. Cermak, S. C. Wasserman, and S. R. Manalis. High-speed multiple-mode mass-sensing resolves dynamic nanoscale mass distributions. *Nature Communications*, 6, 2015. ISSN 20411723 (ISSN). doi: 10.1038/ncomms8070.

[26] Alper Demir and M. Selim Hanay. Fundamental sensitivity limitations of nanomechanical resonant sensors due to thermomechanical noise. *IEEE Sensors Journal*, 20(4):1947–1961, 2020. ISSN 1530-437X 1558-1748 2379-9153. doi: 10.1109/jsen.2019.2948681.

[27] Zurich Instruments. Uhf user manual. Manual, Zurich Instruments, 2020.

[28] Zurich Instruments. Principles of lock-in detection and the state of the art. White paper, Zurich Instruments, 2016. URL `https://www.zhinst.com/europe/resources/principles-lock-detection`.

[29] Eusebius J. Doedel, Alan R. Champneys, Thomas F. Fairgrieve, Yuri A. Kuznetsov, Bjorn Sandstede, and Xianjun Wang. Auto 97: Continuation and bifurcation software for ordinary differential equations (with homcont), 1998.

[30] Daniel J. Inman. *Engineering Vibrations, International Edition*. Pearson Education Limited, Harlow, 2013. ISBN 9780273785217.

[31] Farbod Alijani. Lecture 6: Weakly nonlinear oscillators. Nonlinear Dynamics lecture slides, 2019.

[32] Farbod Alijani. Lecture 7: Forced nonlinear oscillators. Nonlinear Dynamics lecture slides, 2019.

[33] Ali Hasan Nayfeh and Dean T. Mook. *Nonlinear Oscillations*. Wiley, 1995. ISBN 97804711214286. doi: `10.1002/9783527617586`.

[34] Ebrahim Esmailzadeh, Davood Younesian, and Hassan Askari. *Analytical methods in nonlinear oscillations : approaches and applications*. Solid Mechanics and Its Applications. Springer, Dordrecht, Netherlands, 2019. ISBN 9789402415421. doi: `10.1007/978-94-024-1542-1`.

[35] S. H. Strogatz. *Nonlinear Dynamics and Chaos: With Applications to Physics, Biology, Chemistry, and Engineering*. Westview Press, 2nd edition, 2014. ISBN 978-0813349107.